Suppressing Near-Surface Reverse Time Migration Artifacts
Using a Band-selecting Imaging Condition

By

Yao Wang

Submitted to the graduate degree program in Geology and the Graduate Faculty
of the University of Kansas in partial fulfillment of the requirements
for the degree of Master of Science.

_____
Chairperson Richard D. Miller

_____
Douglas Walker

_____
Georgios P. Tsoflias

_____
Ross Black

Date Defended: 5-12-2015

The Thesis Committee for Yao Wang

Certifies that this is the approved version of the following thesis:

Suppressing Near-Surface Reverse Time Migration Artifacts

Using a Band-selecting Imaging Condition

Chairperson Richard D. Miller

5-12-2015

Date Approved

Abstract

In this paper, I introduce a frequency band-selecting imaging condition for Reverse Time Migration (RTM) of shallow reflection datasets which effectively eliminates artifacts that are problematic on near-surface reflection sections. Within the classically defined near-surface region of the subsurface, standard applications of RTM suffer from low-spatial-frequency artifacts, which are obvious for settings where the impedance contrast is sharp or where the shallow structure is complex. The principal reason for this phenomenon is that commonly used RTM imaging conditions—the cross-correlation imaging condition and Poynting vector imaging condition—do not take into account the fact that near-surface datasets commonly have broad frequency bands. The solution to this problem is application of a band-selected imaging condition. The band-selected imaging condition applies a spatially dependent band-pass filter to both the forward-propagating wavefield and the backward-propagating wavefield at each imaging grid point before the cross-correlation of these two wavefields. Since resolution of migrated seismic data is a function of frequency, this imaging condition minimizes the negative impact on resolution most high-resolution migrated data suffer. The utility of this method and improvement in imaging quality is demonstrated with examples of synthetic and real shallow reflection data. Numerical examples demonstrate the notable effect on resolution and artifacts with the band-selection imaging condition compared to the cross-correlation imaging condition and Poynting vector imaging condition. This new method of RTM clearly demonstrates on real data a mechanism for maintaining data resolution while increasing the accuracy of fine structure details interpreted on shallow reflection data.

Acknowledgements

I am so thankful for all of the kind support I received that helped me go through hardness. I would like to express my thanks of gratitude to my advisor Rick Miller for his support and inspiration. To my committee members and professors, for being patient in teaching, guiding and advising. To everyone who worked with me at the Kansas Geological Survey, especially Shelby Peterie for her assistance in work, Julian Ivanov for his support in programming, and Brett Judy for his nice work in data processing. Above all, I am so grateful for my parents.

TABLE OF CONTENTS

TABLE OF FIGURES

1 - Introduction

Reverse time migration (RTM) is an imaging technique that is based on the time-reversal property of the two-way wave equation. With this property, the forward-propagating source wavefield and the backward-propagating receiver wavefield are considered symmetrically identical in the time dimension. RTM is a wave equation migration method with no approximations or dipping angle limitation. RTM involves propagating data both downward (forward-propagating source wavefield) and upward (backward-propagating receiver wavefield) through the geologic model. If the model is correct, the downward-propagating and upward-propagating wavefields will meet each other at the reflecting point. Thus, reflectors can be imaged by summing the cross-correlation of the downward-wavefield and upward-wavefield over the entire recording time period (Claerbout, 1984). Several successful implementations of RTM using this imaging condition have been reported for exploration seismic data (Baysal et al., 1983; Kosloff and Baysal, 1983; McMechan, 1983).

A principal challenge in applying RTM is the low-spatial-frequency artifacts. These artifacts are commonly produced as a result of interference between the source and receiver wavefields. One way to resolve this problem is to image decomposed wavefields separately. According to the propagation direction on the reflector, the wavefield can be decomposed into reflected wavefield and transmitted wavefield. Etgen (1986) and Baysal et al. (1984) introduced a weak-reflection wave equation to attenuate the interference between wavefield components near interfaces. Building on their equation, Fletcher et al. (2006) applied a directional damping term at interfaces to attenuate reflections. According to the elastic dynamic modes the wavefield can be decomposed into compressional wavefield and shear wavefield. Liu et al. (2011) proposed an imaging condition that is based on this kind of decomposition of the wavefield. The main

advantage of the wavefield decomposition method is it reduces artifacts by preventing their emergence. This method treats useful information as noise, however, and many times signal gets suppressed (Diaz and Sava, 2012).

Another approach is to use updating imaging conditions. Chang and McMechan (1986) developed an excitation-time imaging condition that reduces artifacts produced by cross-correlation, but this method could be unstable when the velocity model is not smooth. Guitton et al. (2006) introduced a least-square filter to attenuate the low-spatial-frequency noise in the migration result. This method is both effective and economic. For near surface applications, however, RTM artifacts from shallower reflections may overshadow (or illuminate) subsequent reflections, so applying a least-square filter may attenuate reflection information. Yoon and Marfurt (2006) used the Poynting-vector imaging condition as an expansion of Laplacian filtering. Fleury (2010) used an imaging condition built around scattering-based image-domain interferometry to dampen nonlinear scattering effects. Applying new imaging conditions does not change the behavior of the wavefield nor does it delete useful signals. These methods are all effective in addressing various problems, but none addresses the bandwidth limiting artifacts that plague shallow reflection data.

2 - Problems

Despite the wide application of RTM on conventional exploration seismic data, only a limited number of near-surface seismic RTM cases have been reported. This scarcity of reported applications is likely related to a lack of options for dealing with near-surface issues that must be taken in account when applying RTM. One of these issues is the fact that the near-surface reflection data have broad frequency bands. **Figure 1** presents typical exploration seismic data and a shallow reflection data. **Figure 2** shows the frequency spectra of the two data sets, respectively. From these figures it can be observed that, compared to exploration seismic data, shallow reflection data have

a broader frequency band and higher upper usable corner frequency. Moreover, the shallow reflection data do not have a dominant frequency like what is common for exploration seismic datasets (**Figure 2a**). These broadband frequency signals make the cross-correlation imaging condition inadequate.

Low frequencies possess long wavelengths that are insensitive to shallow reflectors with small layer intervals, while high frequency signal contains reflection information from shallower or thinner reflectors. For most shallow reflection environments, cross-correlating high-frequency reflection signals with their coherent low-frequency components will produce artifacts. Such artifacts may reduce the resolution of image near complex structures and sharp impedance contrast. Another issue is that shallow reflection seismic data contain multiple wave modes and coherent noise events within the optimum reflection recording window. As a result, shallow reflection data are often highly processed in attempts to mute the noise arrivals or to enhance the reflection signal. After such noise suppression or signal enhancement processes the frequency spectrum is whitened, which implies that additional rebalancing of frequency components is needed. Considering these two issues, directly using the cross-correlation imaging conditions on near-surface data may lead to severe artifacts due to the low-frequency trend of the method and high-frequency noise. Therefore, new imaging conditions need to be developed that take into account the frequency characteristics of near-surface data.

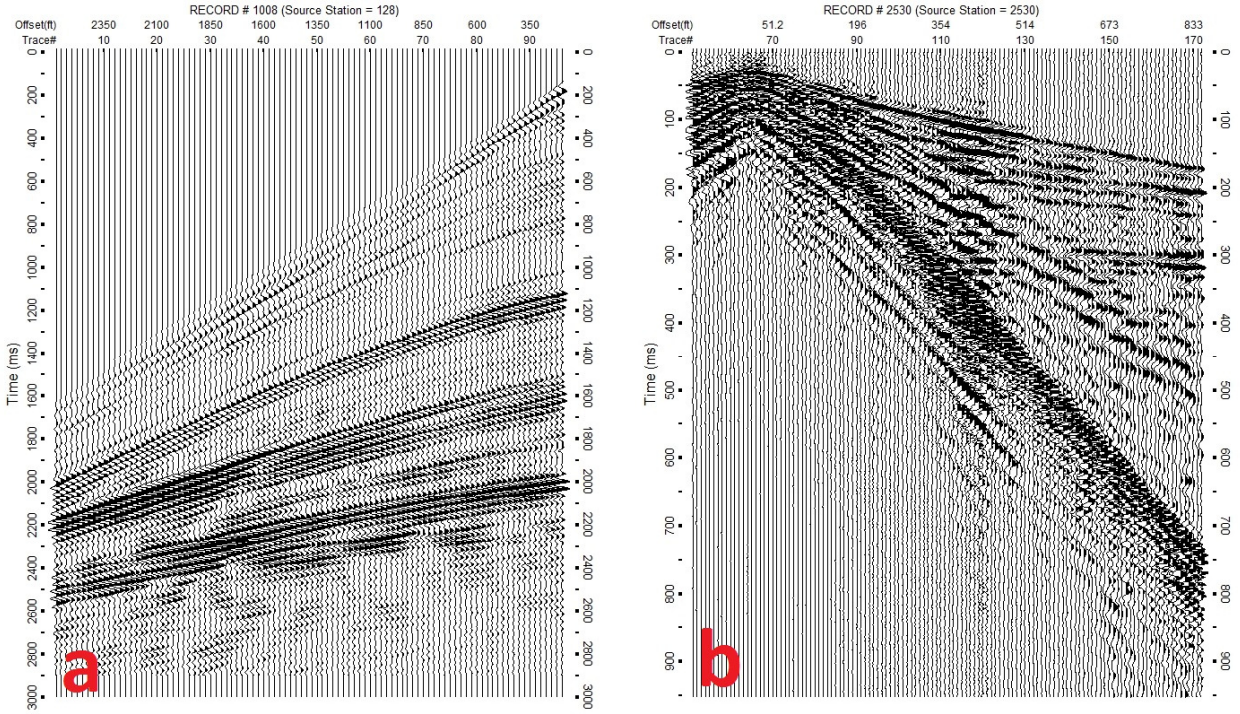

Figure 1. Comparison of (a) a typical exploration seismic data with (b) a near-surface seismic data.

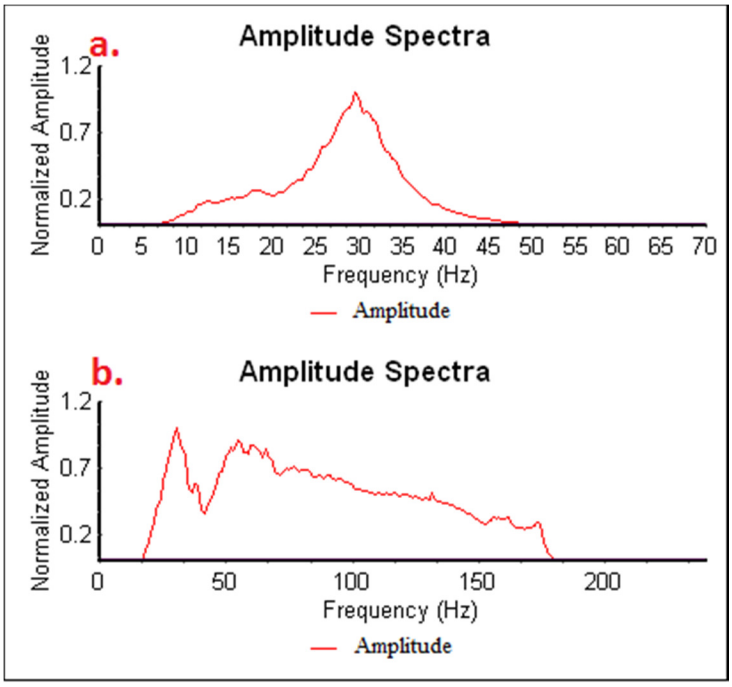

Figure 2. (a) Spectrum of a typical exploration seismic data (Figure 1a). The frequency band is bounded between 5 Hz and 50 Hz and it has a peak value that appears near 30 Hz. (b) Spectrum of a near-surface seismic data (Figure 1b). This data has a wide spectrum range from 20 Hz to 180 Hz.

The Poynting-vector imaging condition (Yoon and Marfurt, 2006) is a technique used in the seismic exploration industry to suppress artifacts produced through reducing the cross-talk (interference) generated at interfaces between the transmitting wavefield and the reflecting wavefield. This method applies a weighting function to the image that is defined by the incidence angle of each ray at each image point. The power fluxes (i.e., Poynting vectors) of forward- and backward-wavefields are used to calculate the incidence angle. Because this method does not specify or limit the frequency band of signal used for imaging, it cannot reduce artifacts associated with near-surface reflections due to RTM. In chapter 4, numerical examples are used to demonstrate that Poynting-vector imaging is inadequate for attenuating near-surface artifacts.

In this research, I solve the problems of near-surface artifacts resulting from the extended frequency band of shallow reflections. I introduce a new spatially dependent frequency band selected imaging condition for near-surface RTM that dramatically extends the resolution and accuracy of interpreted structures. This new imaging condition will be applied to both synthetic and real shallow reflection datasets to theoretically and empirically demonstrate its effectiveness in suppressing these near-surface artifacts. For near-surface problems, though Full-Waveform Inversion (FWI) methods are more efficient, migration methods can provide results with more detail, improved resolution, and less uncertainty (Berkhout, 2012)—even for images of the shallow subsurface—than images without migration. So with this research I have developed an enhancement to the RTM method based on the band-selecting imaging condition that has proven to improve resolution in near-surface reflection data.

3 - Geophysics

3.1 RTM Algorithm and Imaging conditions

The RTM algorithm uses the downward-going source wavefield and the upward-going receiver wavefield to image reflectors. This imaging process is subject to a zero-lag cross-correlation imaging condition (Claerbout, 1984), and is shown as

$$I(\boldsymbol{x}) = \int_0^{t_{max}} G_s(\boldsymbol{x},\tau) G_r(\boldsymbol{x},\tau)\, d\tau = \sum_{t=0}^{t_{max}} G_s(\boldsymbol{x},t) G_r(\boldsymbol{x},t). \qquad (1)$$

Where G_s and G_r are the down-going source wavefield and up-going receiver wavefield, respectively. $I(\mathbf{x})$ is the image amplitude at the grid point $\mathbf{x} = (x, z)$ in 2-D space and $\mathbf{x} = (x, y, z)$ in 3-D space. t_{max} is the maximum recording time. The wavefields can be obtained by using either finite-difference or finite-element methods in both time and frequency domains. The wavefields obtained in this way include both propagation directions and all possible scattering angles. Therefore, no approximation is made during the imaging process and thus high-resolution results are possible.

The Marmousi velocity model (**Figure 3**) and data provided by Institut Français du Petrole (IFP) in 1993 is a benchmark for testing migration algorithms. This velocity model has structural and velocity complicities which are difficult to accurately image. The complexities designed into the synthetic data are easily identified in migration results (**Figure 4a**). Severe artifacts occur when using the cross-correlation imaging condition in RTM within the near-surface, and those artifacts mask subsequent layers within what can only be termed as a shadow zone. This phenomenon can dramatically hamper interpretation, especially for cases with only shallow layers or where the shallow layers are the main target. More details will be given and discussed with numerical examples in chapter 4.

To reduce or eliminate these shallow artifacts, the wavefield must be decomposed to reduce interference between components or modes of the wavefield. At the reflecting interface, the wavefield can be decomposed into reflecting (-) and transmitting (+) components as

$$G_s(\boldsymbol{x},t) = G_{s+}(\boldsymbol{x},t) + G_{s-}(\boldsymbol{x},t), \tag{2}$$

$$G_r(\boldsymbol{x},t) = G_{r+}(\boldsymbol{x},t) + G_{r-}(\boldsymbol{x},t). \tag{3}$$

Substituting equation (2) and (3) into equation (1) to get

$$I(\boldsymbol{x}) = \sum_{t=0}^{t_{max}} [G_{s+}(\boldsymbol{x},t)G_{r+}(\boldsymbol{x},t) + G_{s-}(\boldsymbol{x},t)G_{r+}(\boldsymbol{x},t) + G_{s+}(\boldsymbol{x},t)G_{r-}(\boldsymbol{x},t) + G_{s-}(\boldsymbol{x},t)G_{r-}(\boldsymbol{x},t)]. \tag{4}$$

The imaging result (4) has multiple terms. If the geological model used for migration is correct, all these terms will reach their maximums at the scatter's position in the image grid. Since migration and imaging are recursive processes, it is not valid to assume the model is always correct. Interference between these main terms is a main source of near-surface RTM artifacts when an inaccurate model is used.

The method I propose reduces the number of terms of equation (4) and therefore the opportunities for these terms to produce components that interfere. During the extrapolation of the receiver wavefield, I use a nonreflecting acoustic wave equation (Baysal et al., 1984) to eliminate the reflection events from a narrow reflecting angle. Then I apply the Poynting-vector imaging condition (Yoon and Marfurt, 2006) to mute wide-angle reflecting events.

The nonreflecting acoustic wave equation in 2-D space is

$$\partial_t^2 P = c^2(\partial_{\mathrm{x}}^2 + \partial_{\mathrm{z}}^2)P + c(\partial_{\mathrm{x}}, \partial_z)P \cdot (\partial_{\mathrm{x}}, \partial_z)c, \tag{5}$$

where P is acoustic pressure, c is pressure wave velocity. Equation (5) is still a two-way wave equation. This equation has limited effectiveness in suppressing reflecting waves with an angle of

incidence. Increasing the incidence angle allows the reflections to appear again. To dampen the wide-angle reflections I applied the Poynting-vector imaging condition

$$I(\boldsymbol{x}) = \int_0^{t_{max}} \cos^{\mathrm{n}}\theta\, G_s(\boldsymbol{x},\tau) G_r(\boldsymbol{x},\tau)\, d\tau = \sum_{t=0}^{t_{max}} \cos^{\mathrm{n}}\theta\, G_s(\boldsymbol{x},t) G_r(\boldsymbol{x},t). \qquad (6)$$

In equation (6) the classical cross-correlation imaging condition is multiplied by an incidence-angle-dependent coefficient $\cos^{\mathrm{n}}\theta$. The incidence angle θ is defined by

$$cos\theta = \frac{\boldsymbol{\varepsilon}^s \cdot \boldsymbol{\varepsilon}^r}{|\boldsymbol{\varepsilon}^s||\boldsymbol{\varepsilon}^r|}, \qquad (7)$$

and

$$\boldsymbol{\varepsilon} \cong -\boldsymbol{v}P = -\nabla P \frac{dP}{dt} P, \qquad (8)$$

where $\boldsymbol{\varepsilon}$ is the power flux (the rate of power transfer per unit area) vector of the wavefield at a grid point, $\boldsymbol{v}$ is the ray direction vector, and P is the pressure. ∇ is the Nabla (del) operator that in 2-D is $\nabla = (\partial_{\mathrm{x}}, \partial_{\mathrm{z}})$ and in 3-D it is $\nabla = (\partial_{\mathrm{x}}, \partial_{\mathrm{y}}, \partial_{\mathrm{z}})$. The incidence angle θ can be determined by computing the power flux of the source-wavefield and receiver-wavefield. An incidence-angle-dependent coefficient can be used to dampen wide-angle reflections.

After applying these two techniques, theoretically we have $G_{s-} = 0$ and $G_{r-} = 0$, and in equation (4) all terms containing each of these two elements were removed. Then the imaging result becomes

$$I(\boldsymbol{x}) = \sum_{t=0}^{t_{max}} G_{s+}(\boldsymbol{x},t) G_{r+}(\boldsymbol{x},t). \qquad (9)$$

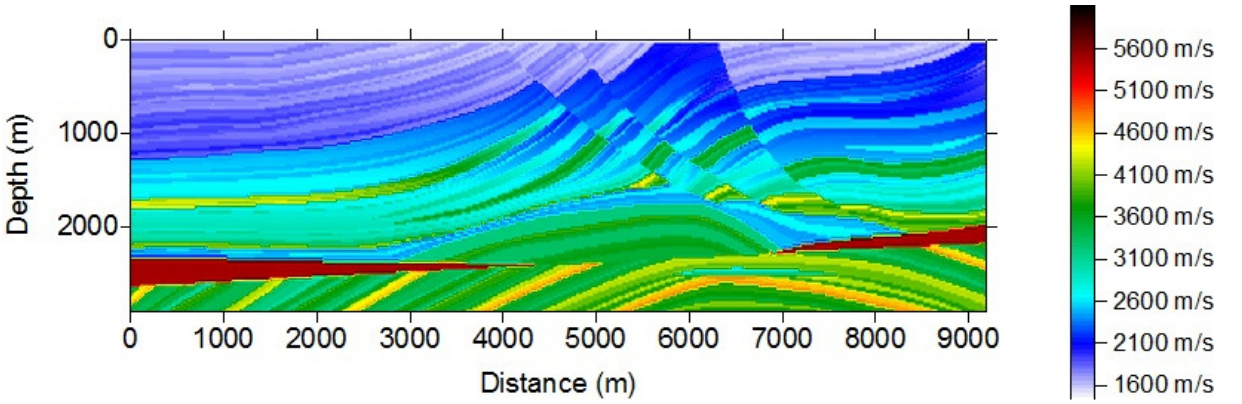

Figure 3. The Marmousi velocity model.

This wavefield-decomposition method has garnered success producing high-resolution preliminary results with exploration seismic datasets (**Figure 4**). Both the Poynting-vector imaging condition and application of the Poynting-vector imaging condition with the nonreflecting wave equation can suppress the migration artifact in conventional data sets.

For conventional exploration seismic data sets, as described in chapter 2, the reflection signals are within a frequency band that is not susceptible to the high frequency artifacts observed on shallow data sets. For example, In **Figure 1a** and **Figure 2a**, the frequency of the displayed typical exploration seismic gather is from 5 Hz to 50 Hz with a peak value near 30 Hz. As a result, the thickness of most of the reflectors are less than quarter of the reflecting waves' wavelengths, which is the limitation of vertical resolution (Yilmaz, 2001, Page 1801), assuming normal velocity rock. With this characteristic, the reflecting angle with this rock interval can be computed correctly. For shallow reflection cases (**Figure 1b** and **Figure 2b**), because the low-frequency components have wavelengths greater than the limit of vertical resolution, reflecting angles are generally computed incorrectly and thus the Poynting-vector imaging condition likely will not improve the quality (accuracy or resolution) of the image significantly. To more fully illustrate this point, a numerical example is presented later in chapter 4. That example demonstrates clearly that the Poynting-vector imaging condition is inadequate for shallow reflection data.

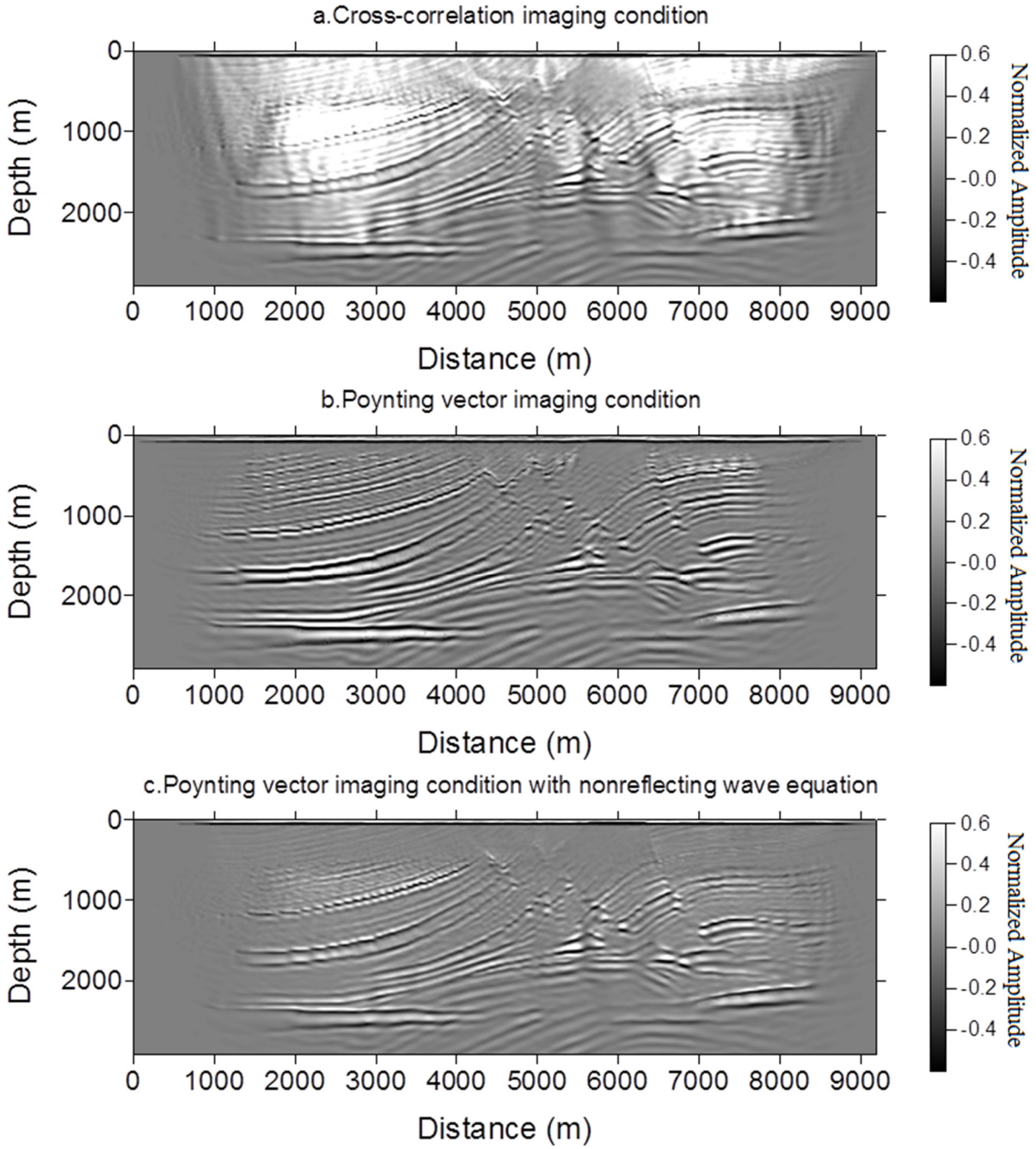

Figure 4. Examples of RTM of a synthetic data set using the Marmousi velocity model. Each result was normalized by its maximum absolute value. (a) RTM result from using the cross-correlation imaging condition. (b) The result from using Poynting-vector imaging condition. (c) The result from using Poynting-vector imaging condition with a nonreflecting wave equation.

3.2 Band-selecting Imaging condition

Previous discussion and models have shown that the cross-correlation imaging condition and the Poynting-vector imaging condition return acceptable results for exploration seismic

datasets. These two imaging conditions use the full spectral bandwidth contained in the data for imaging. Within the near-surface, where reflections wavelets are commonly high-frequency components (Sheriff 2002) of the wavefield, cross-correlating coherent low-frequency components that are not reflections will produce artifacts and reduce resolution of the processed seismic section. The wavefield can be decomposed relative to the direction of propagation and the frequency. I use a frequency band-selecting imaging condition for segmenting frequency bands within shallow reflection datasets. The forward-propagating wavefield is cross correlated with the backward-propagating wavefield before the spectral partitioning. These two cross-correlated wavefields were filtered by spatial-dependent filters to choose ideal frequencies best segregated for shallow imaging. In the frequency domain, (1) becomes

$$I(\boldsymbol{x}) = \sum_{\omega} \overline{G_s(\boldsymbol{x}, \omega)} \cdot G_r(\boldsymbol{x}, \omega). \tag{10}$$

Two filtered traces can be used to strengthen the reflection signal within a certain frequency band. In a frequency band defined by $\{f | \omega_a \leq f \leq \omega_b\}$, let

$$\eta = \frac{\|\omega_a + \omega_b\|}{2}, \tag{11}$$

$$\xi = \|\omega_a - \eta\|, \tag{12}$$

where η is the central frequency and ξ is the bandwidth. Then, when properly chosen for the near-surface, η and ξ effectively suppress near-source artifacts. This is demonstrated with the numerical examples in the following sections.

This imaging condition is easy to implement if the wavefield extrapolation is performed in the frequency domain

$$I(\boldsymbol{x}) = \sum_{shot} \sum_{\omega} h(\eta, \xi, \boldsymbol{x}) \overline{G_s(\boldsymbol{x}, \omega_\iota)} \cdot g(\eta, \xi, \boldsymbol{x}) G_r(\boldsymbol{x}, \omega_i), \tag{13}$$

where $h(\eta, \xi, \boldsymbol{x})$and $g(\eta, \xi, \boldsymbol{x})$ are spatially-dependent filters designed for the source wavefield and receiver wavefield, respectively. For convenience, we can set $h(\eta, \xi, \boldsymbol{x}) = g(\eta, \xi, \boldsymbol{x})$. Consider the vertical resolution

$$d \geq \frac{\lambda}{4} = \frac{v}{4f} \tag{14}$$

where d is the thickness of the reflector and v is the interval velocity at the reflector's location, with λ the wavelength and f the frequency. Thus the band-pass frequency can be defined by

$$\frac{v}{4d} \leq f \leq \frac{2v}{4d} \tag{15}$$

In this research I let the high-cut frequency be double that of the low-cut frequency, a designation that is based on experience. This band-pass frequency f is spatially dependent because both d and v are dependent on the velocity model. With that established, η and ξ can be defined as

$$\eta = \frac{3v}{8d} \tag{16}$$

$$\xi = \frac{v}{8d} \tag{17}$$

In practice, the velocity model will be updated with each iteration so the thickness of each layer changes. This makes the depth model hard to define. To avoid numerical artifacts caused by poorly constrained values of d, it is recommended to fix d as the thickness of the layer of interest. A well log or some experience may be needed at this point in the procedure. Once d is fixed, the band-selecting filter is now a function of velocity.

Thus, the spatial-dependent frequency filter can be defined as

$$h(\eta, \xi, \boldsymbol{x}) = \begin{cases} 1, & \eta - \xi \leq \omega(\boldsymbol{x}) \leq \eta + \xi, \\ 0, & otherwise. \end{cases} \quad (18)$$

Additionally, this filter needs to have a series of time windows added to reduce the Gibbs phenomenon, which leads to artificial oscillations in the results (Baher, 2001, Page 49).

4 - Numerical experiments-synthetic data RTM

In this chapter I will discuss and display a shallow reflection RTM case. The compressional-wave velocity model used for the dataset synthesis is graphically represented in **Figure 5**. This model simulates a 6-layer sedimentary rock system penetrated by a salt dome from the left-bottom corner. The size of this model is 1000 m by 400 m. Thirty shot records were synthesized with a 60 Hz Ricker wavelet. The density is constant (2000 kilogram per cubic meter) within this modeled area.

In the top left portion of the model, a high-velocity layer is embedded in a low-velocity layer. This area is outlined by a black box (**Figure 5**) with an enlargement of this area displayed in **Figure 6**. There are structural complexities and sharp impedance gradients within this area. As a consequence, it is expected that strong multiple-reflected and refracted events will be observed in the synthetic data.

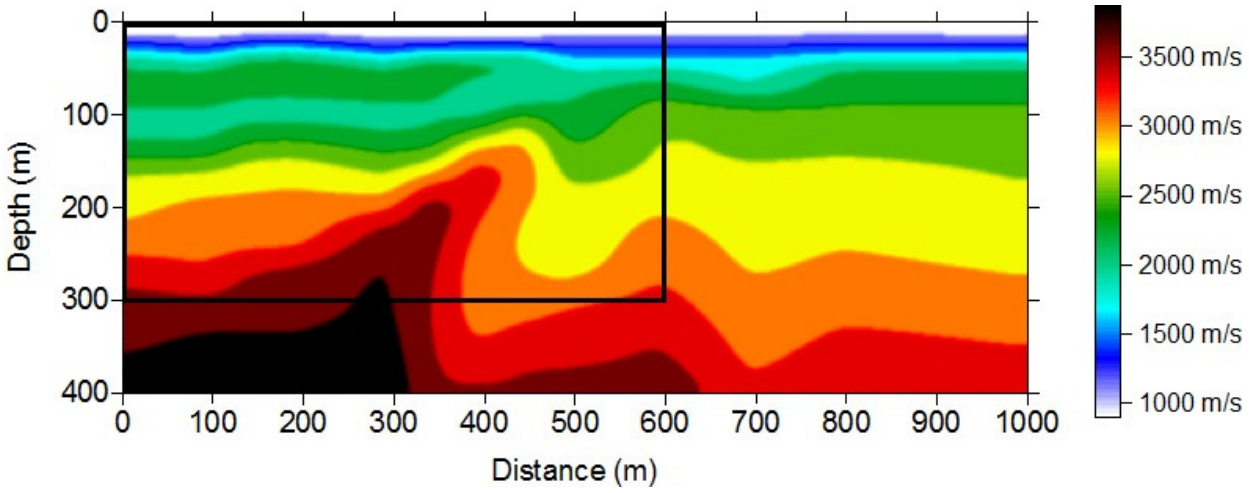

Figure 5. Compressive wave velocity (P-wave velocity) model. The density is constant within this modeled area. A focus area is highlighted by a black solid box.

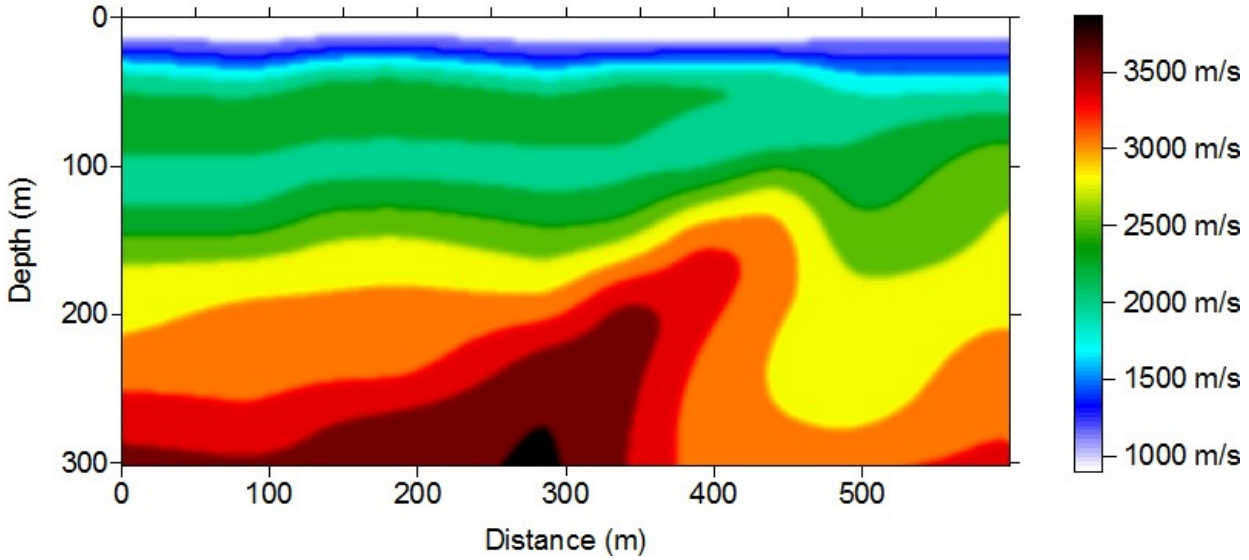

Figure 6. Enlarged section of the P-wave velocity model in Figure 5 between 200 m deep and 600 m offset alone line. This area contains structural and velocity complexities.

Using this part of the velocity model identified by the black box, RTM on one-shot synthetic record (**Figure 7**) was undertaken (**Figure 8**). Low-spatial-frequency artifacts (identified with red arrows in **Figure 8**) are obvious between the top of the high-velocity layer and the source

station, strong evidence supporting the suggestion that the cross-correlation imaging condition and Poynting-vector imaging condition are inadequate at suppressing near-surface artifacts.

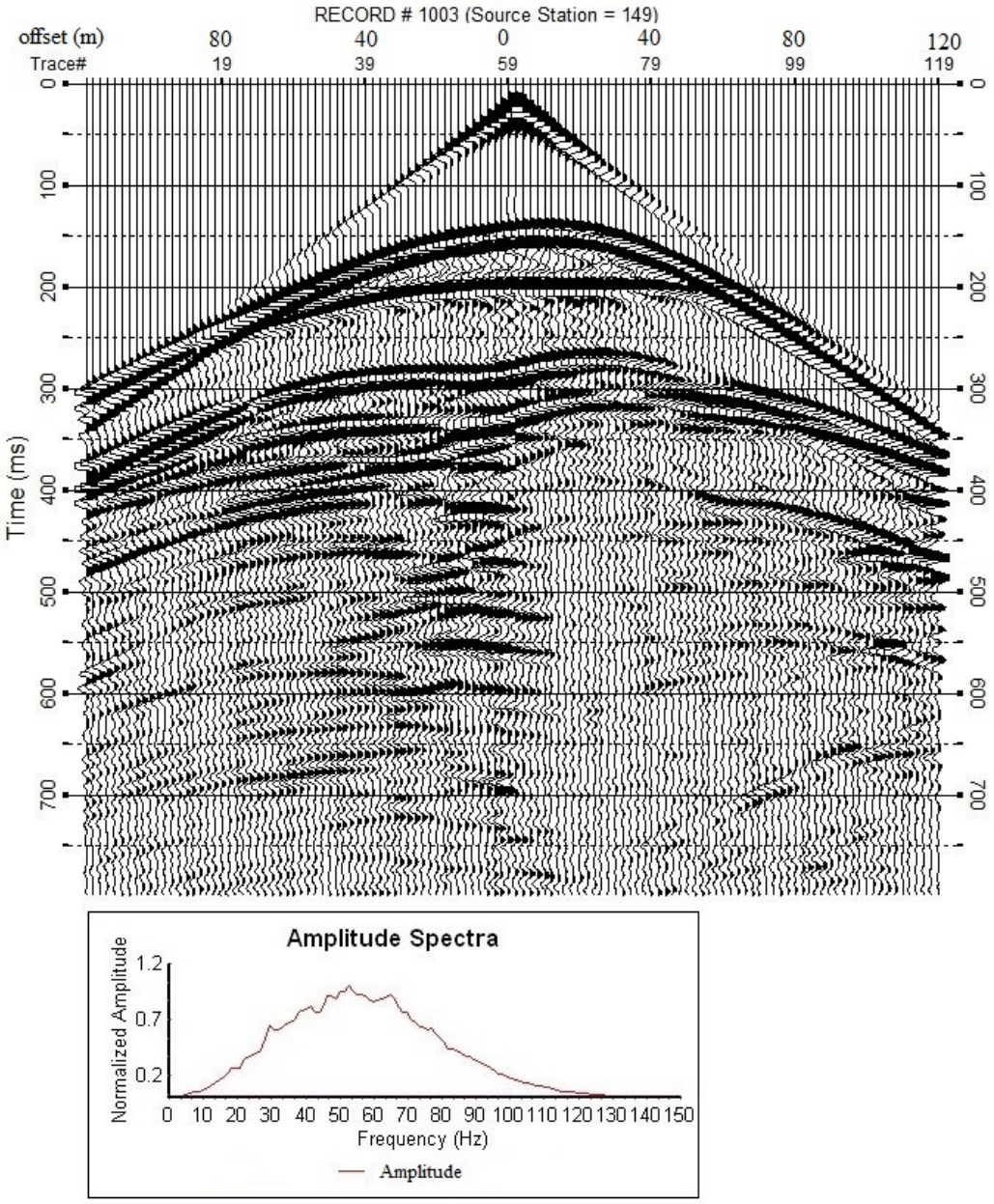

Figure 7. A synthetic record with source station at x=298 m and its frequency spectrum. This record is the 4th record of the synthetic dataset. Each record has 120 channels with 2 m station spacing. The maximum offset for each shot is 120 meters. The spectrum shows that this record has a wide frequency band from 10 Hz to 120 Hz

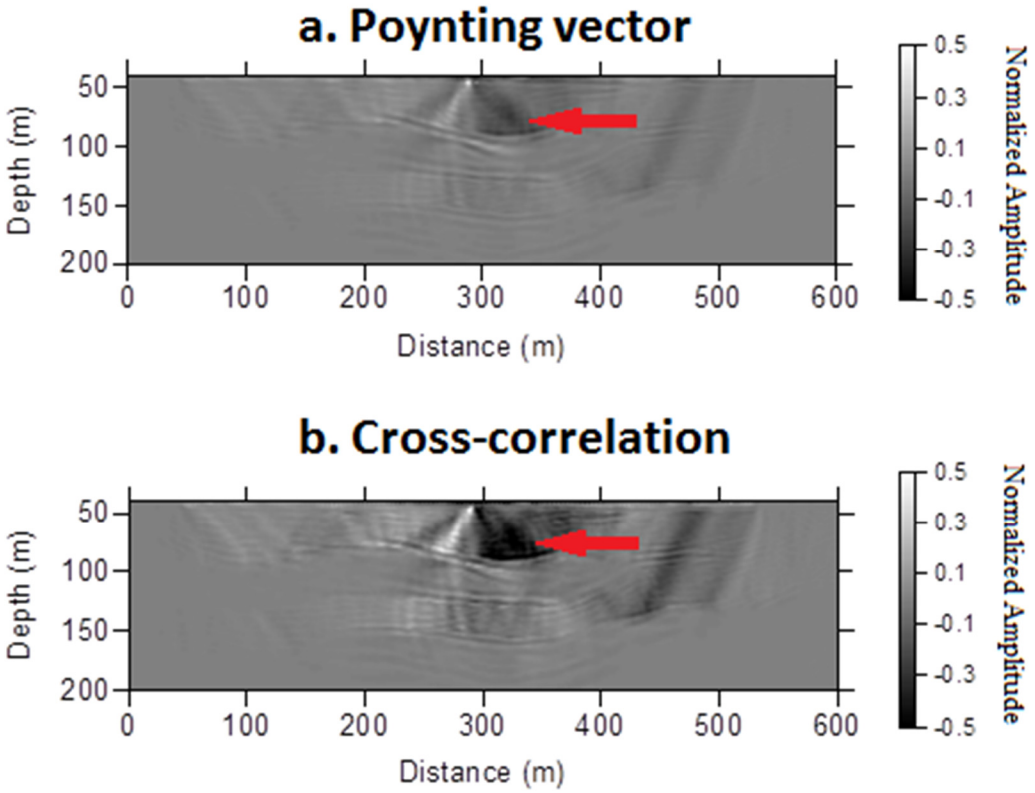

Figure 8. Single shot RTM using (a) Poynting vector imaging condition and (b) Cross-correlation imaging condition respectively. Each result was normalized by its maximum absolute value. Red arrows are showing the artifacts.

Then the band-selecting imaging condition was applied to to the focus area (**Figure 9**) to determine the source of these artifacts. Three frequency bands were defined and used to parameterize the operation. The imaging artifact (identified by red ellipses and arrows in **Figure 9**) is limited to within the second frequency band, suggesting that the near-surface artifacts can be suppressed by selecting the appropriate frequency band at each grid point.

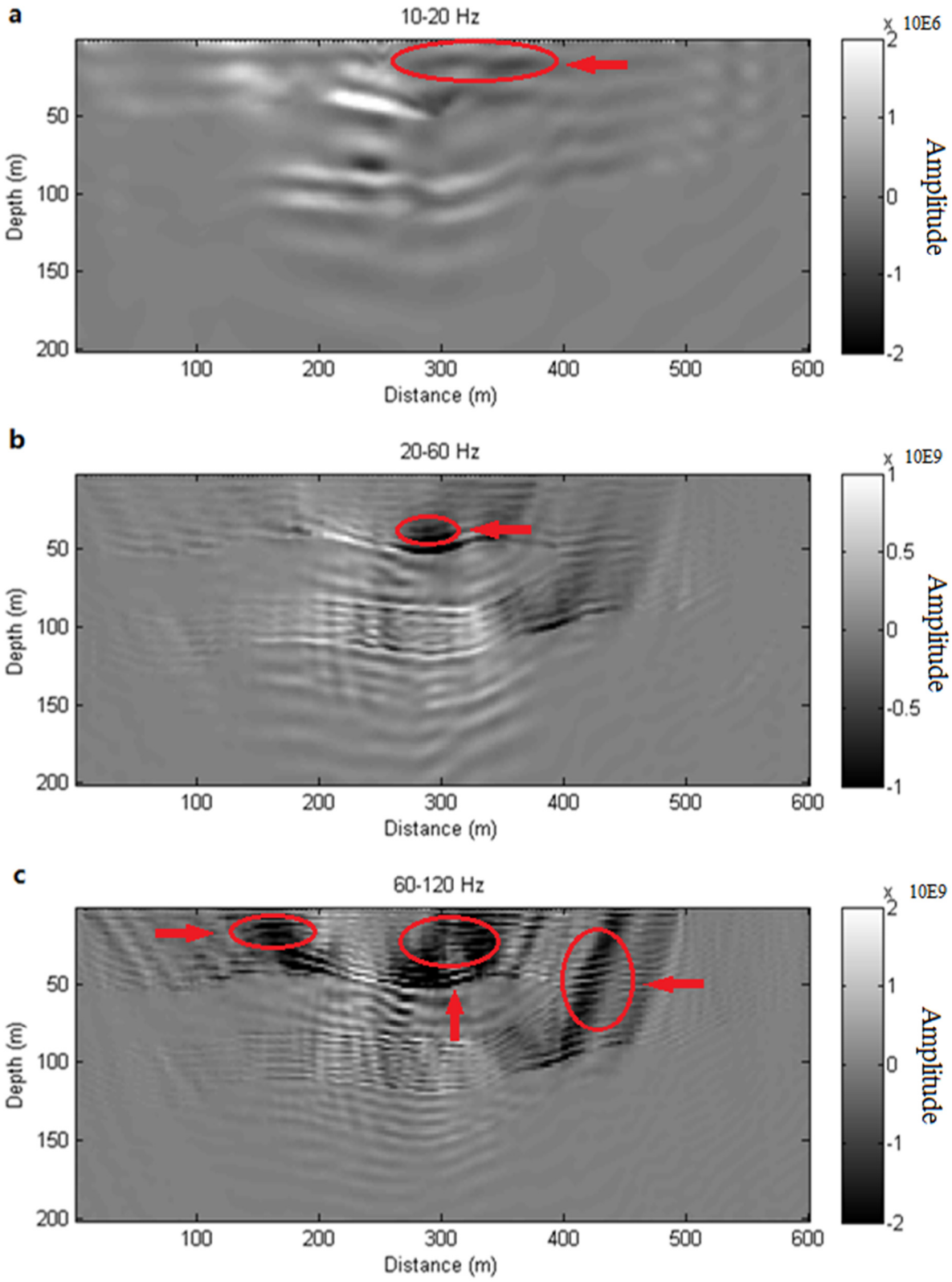

Figure 9. Results of single-shot prestack RTM from a band-selected imaging condition that passes three frequency bands: (a) 10-20 Hz. (b) 20-60 Hz. (c) 60-120 Hz. Artifacts are identified by red ellipses and arrows.

Prestack RTM was performed on the entire dataset (**Figure 10**). The cross-correlation and Poynting-vector imaging condition does not significantly improve the near-surface resolution or suppress artifacts (**Figure 10a** and **Figure 10b**). The band-selected imaging condition however, shows good resolution in the shallow region and minimal artifacts (**Figure 10c**). Here, I fix $d = 50$ m as the threshold of resolution. Using equation (15) with a interval velocity range 2500 m/s ~ 3500 m/s to get the passing band frequency: $15\ \text{Hz} < f < 35\ \text{Hz}$.

I expanded this passing band for applying window functions. The the band-pass filter is spatially independent:

$$h(\eta, \xi, \boldsymbol{x}) = h(\eta, \xi) = \begin{cases} 1, & if\ 10\ Hz \leq \omega \leq 60\ Hz, \\ 0, & otherwise. \end{cases}$$

Therefore, deep reflections are attenuated as a product of the filter design. To compensate, smaller η and larger ξ are selected for the deeper part of the model.

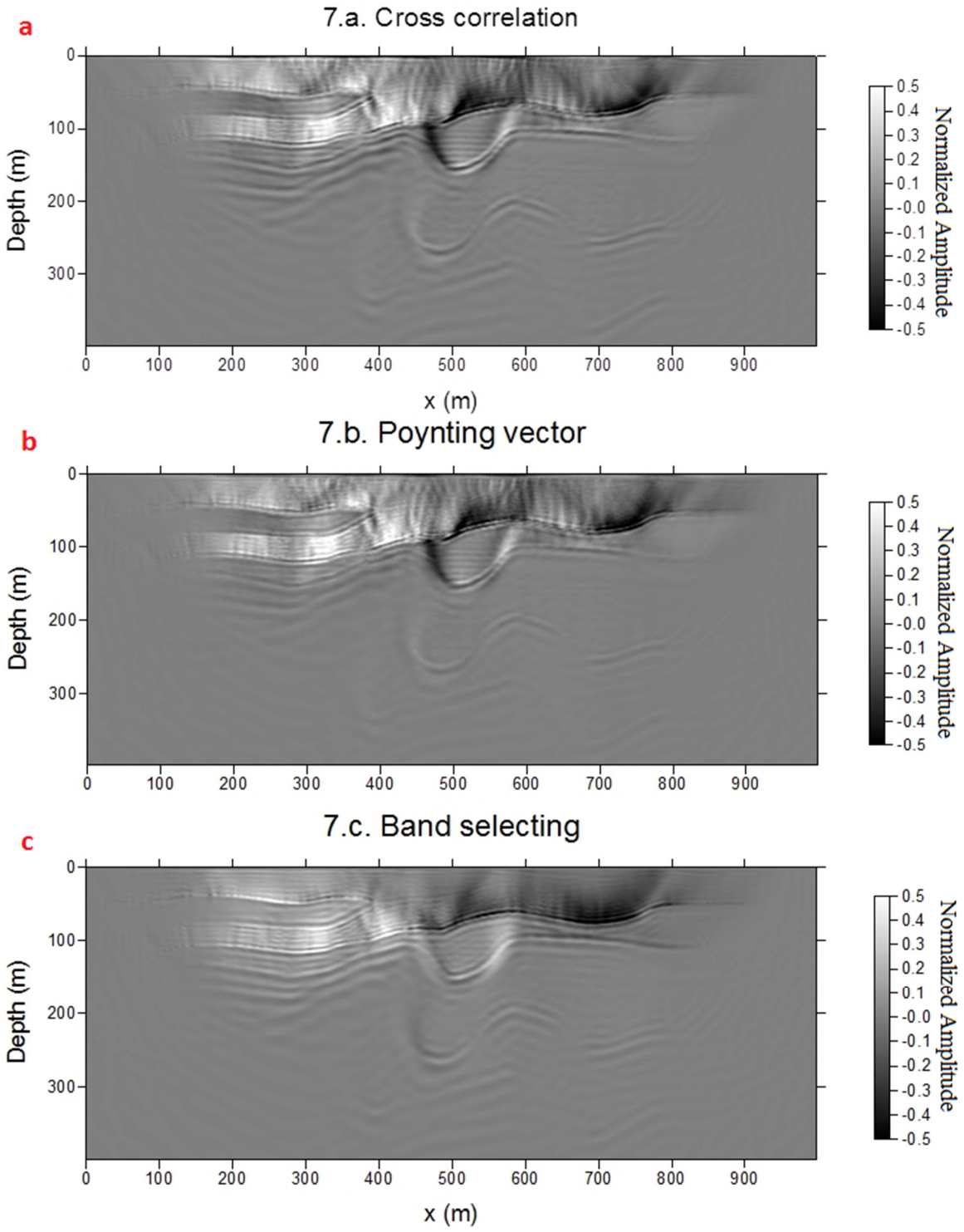

Figure 10. RTM results of the synthetic data set using different imaging conditions. (a) The migration result from applying the cross-correlation imaging condition. (b) The result from Poynting-vector imaging condition. (c) The result from band-selecting imaging condition.

5 - Real data RTM – H3EAST experience

In this section a shallow reflection data set ‘h3east’ will be processed and migrated to test the effectiveness of the band-selecting imaging condition to suppress near-surface artifacts at a site with significant structural variability and extreme interspread velocity variability. This ‘h3east’ data is a part of the dataset collected along U.S. Highway 50 in Reno County (**Figure 11**), Kansas, by the Kansas Geological Survey (KGS) in 2003 and 2008. In 2003, a 10-km section was collected over a region where ground stability had been a concern due to abandoned and unmapped solution mining activities in close proximity to the roadway (Miller and Henthorne, 2004). In 2008, a reflection survey was undertaken to study the Hutchinson Salt Member across the most disturbed portion of the shallow salt, specifically along the eastern dissolution edge, with a focus on better defining the natural processes and migration and drivers.

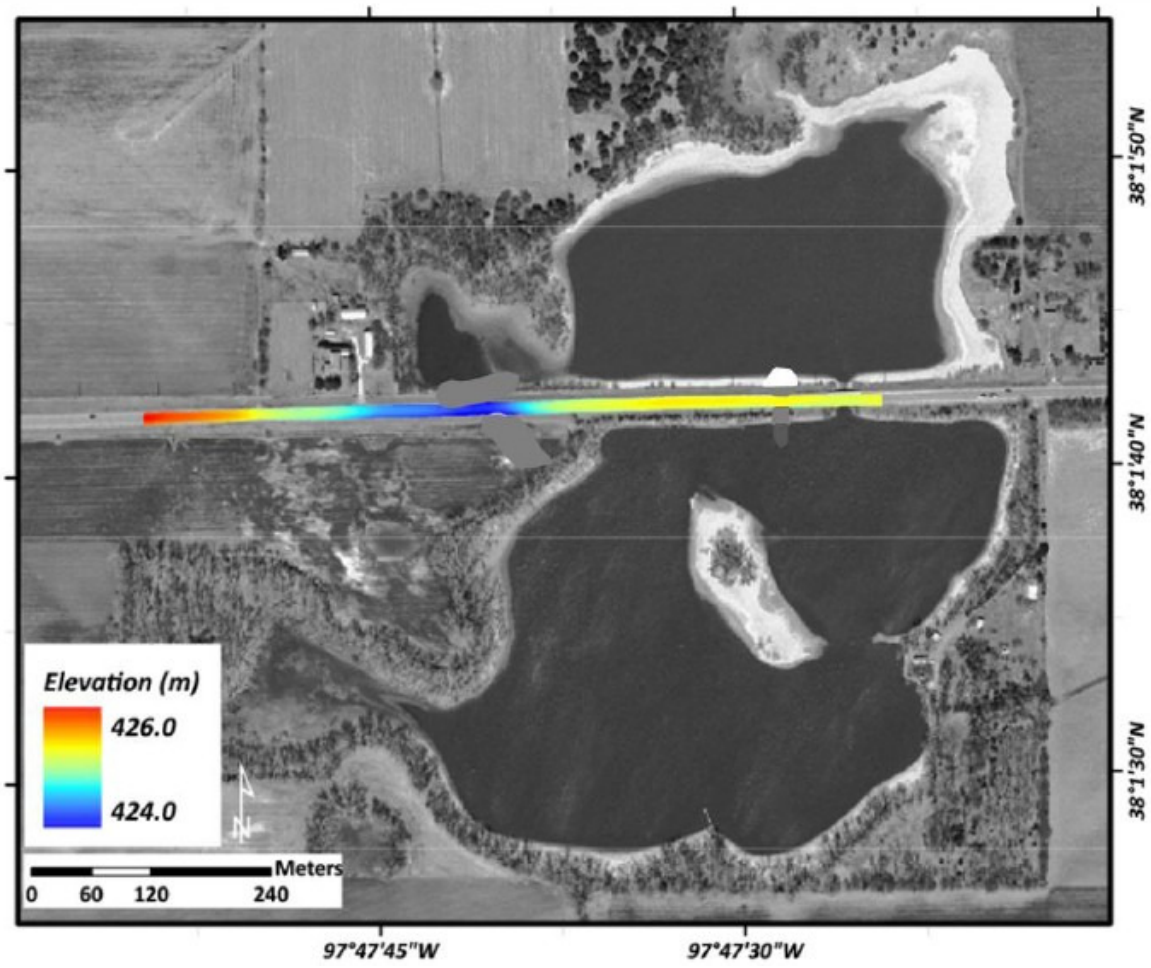

Figure 11. Aerial view image of the survey line. The colored line shows the spread of the survey line. The colors denote the elevation of stations (modified from Judy, 2015).

During the Permian, Kansas was part of a shallow marine shelf sloping to the south with an inlet to the sea. Alternating open marine and stranded sea depositional environments persisted throughout the period (Merriam, 1963). The material deposited during the cyclic sea level change consisted of some sand and silt deposits originating inland, but mostly resulted from a cyclic Permian sea. The stranded nature of the sea resulted in thick evaporate deposits with the open inlet providing new brackish fluid during high sea levels (Merriam, 1963; West et al., 2010).

The interval of interest for this survey is within the Permian Sumner Group in Reno County consisting of the Wellington Formation and the Ninnescah Shale (Norton, 1939). Currently this

sedimentary sequence dips gently to the west within the study area at approximately 6 m/km (Watney et al., 2003). The Wellington Formation can be divided into three contacts identifiable on the seismic data. These contacts are between the lower Wellington member, the Hutchinson Salt member, and the upper Wellington member (Gogel, 1981).

The lower Wellington is largely composed of gray shale but has been described as the "anhydrite beds" (Ver Wiebe, 1937) due to the many cyclical anhydrite layers interbedded within the shale interval. The lower Wellington is largely composed of gray shale with thin anhydrite and gypsum beds (Bayne, 1956; Gogel, 1981). The upper Wellington also is predominantly gray shale with intermittal gypsum, anhydrite, and dolomite (Gogel, 1981). Overlying the Wellington Formation is the Ninnescah Shale, which is considered the bedrock within the study area and is composed of red to reddish-brown shale with some interbedded anhydrite and gypsum (Gogel, 1981). Geology logs from a borehole located immediately west (≈1.5 km) of the 2008 seismic survey place the top of the Chase Group at 265 m, the top of the Hutchinson Salt at 133 m, the top of the Upper Wellington at 80 m, and the top of the Ninnescah Shale at 35 m (**Figure 12**).

The Hutchinson Salt is composed of halite beds ranging from 0.15 to 3 m thick interbedded with laterally discontinuous insoluble beds of shale, anhydrite, and dolomite (Walters, 1978). The salt interval has wide lateral continuity in south-central Kansas; however, the lateral continuity of individual salt beds is less extensive, generally only continuous for a few miles (Dellwig, 1971).

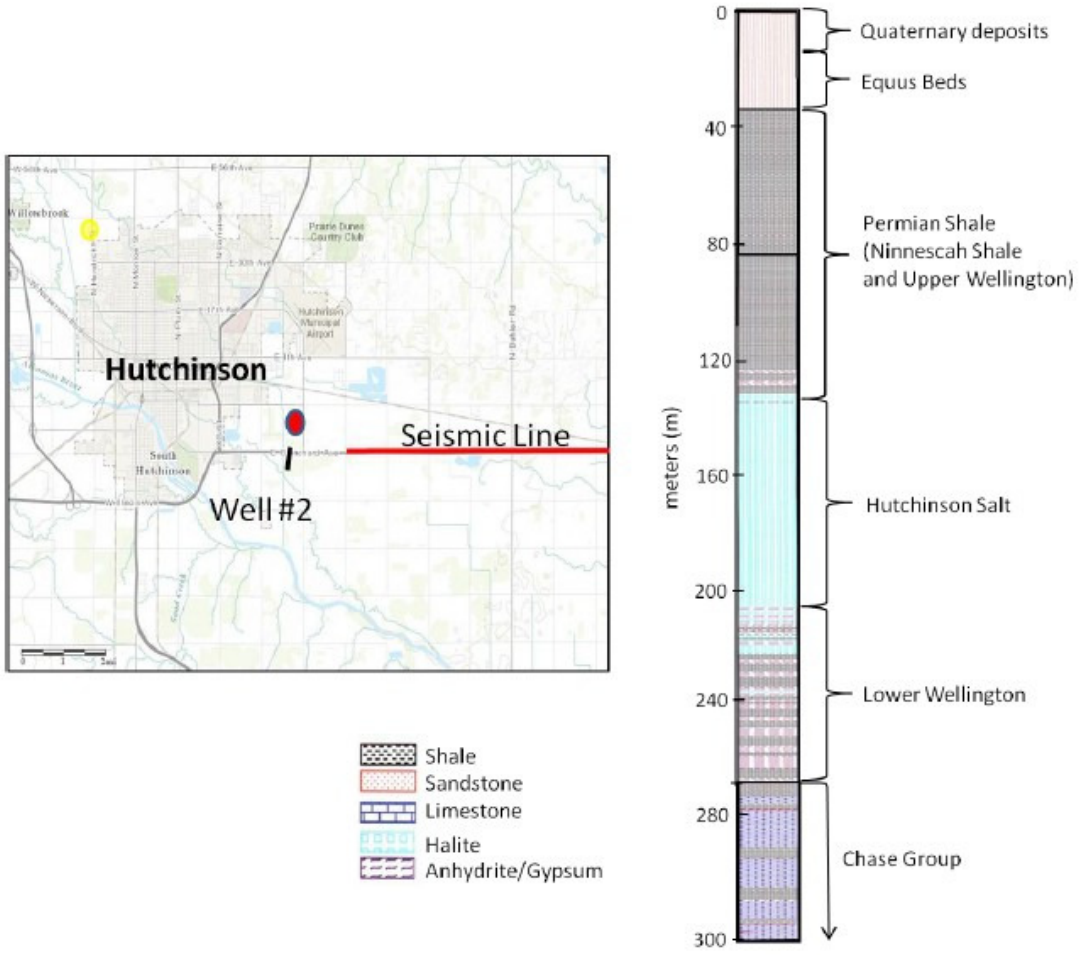

Figure 12. (right) Geology log from well WD#2 owned by the City of Hutchinson indicating depths to Lower Permian units near the area of interest. (left) Map showing well proximity to the 2008 U.S. 50 seismic survey (modified from Judy, 2015).

The 'h3east' vibroseis data set includes 267 vibrator points with each shot record consisting of 240 recording channels. Since the emphasis was on shallow structures, the correlated recording time used here is 0.3 seconds with a sampling interval of 1 millisecond. The receiver station spacing is 2.5 meters and the spacing between adjacent vibrator points is 5 meters. The portion of survey line that includes the 'h3east' data is about 1800 meters in length.

These 'h3east' data were used for testing pre-stack shallow seismic data migration routines because of the very challenging and short wavelength subsidence structures resulting in a complex velocity function. Based on previous processing and interpretations (Judy, 2015) and the geologic

setting, a reasonable initial velocity model was available, and with the challenging structural features observed on F-K migrated sections, these data should really put the migration algorithm I developed through its paces.

5.1 Processing and time migration

A 2-D high resolution vibroseis common-midpoint (CMP) processing flow was utilized (**Figure 13**) (Steeples and Miller, 1998; Miller, 2007). Processing of the data includes muting direct wave and ground roll, frequency filtering, deconvolution, sorting into CMP gathers, normal move out (NMO) correction, trace balancing, and velocity analysis. Data processing was accomplished using software packages developed by the Kansas Geological Survey, Winseis and SeisUtilities. With these processing steps, random noise was suppressed and reflection events enhanced (**Figure 14**). After the NMO correction and velocity analysis, a velocity function was obtained which was then followed by time domain F-K migration of the data, a routine sequence for shallow reflection sections (**Figure 15**).

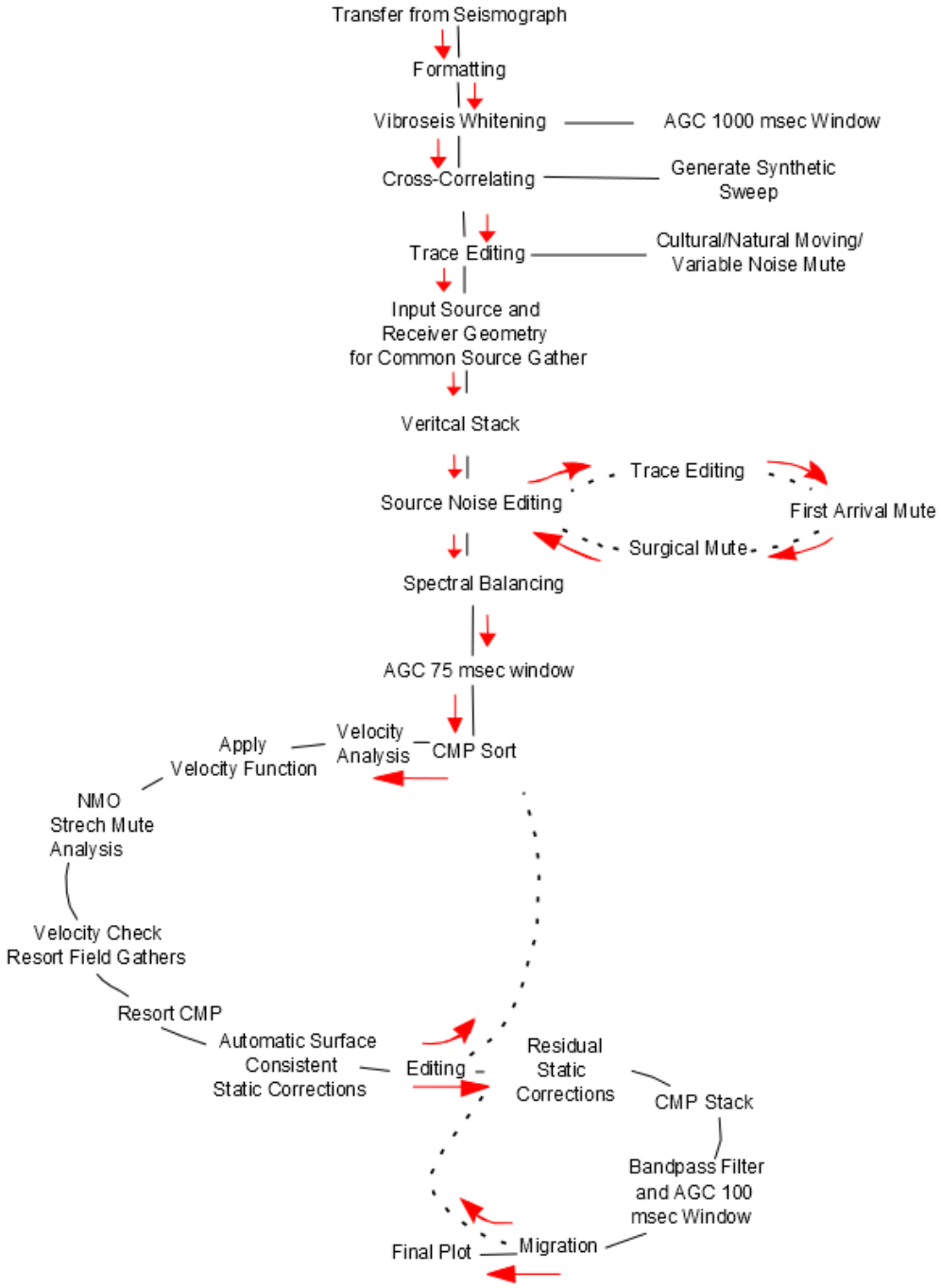

Figure 13. Processing flow.

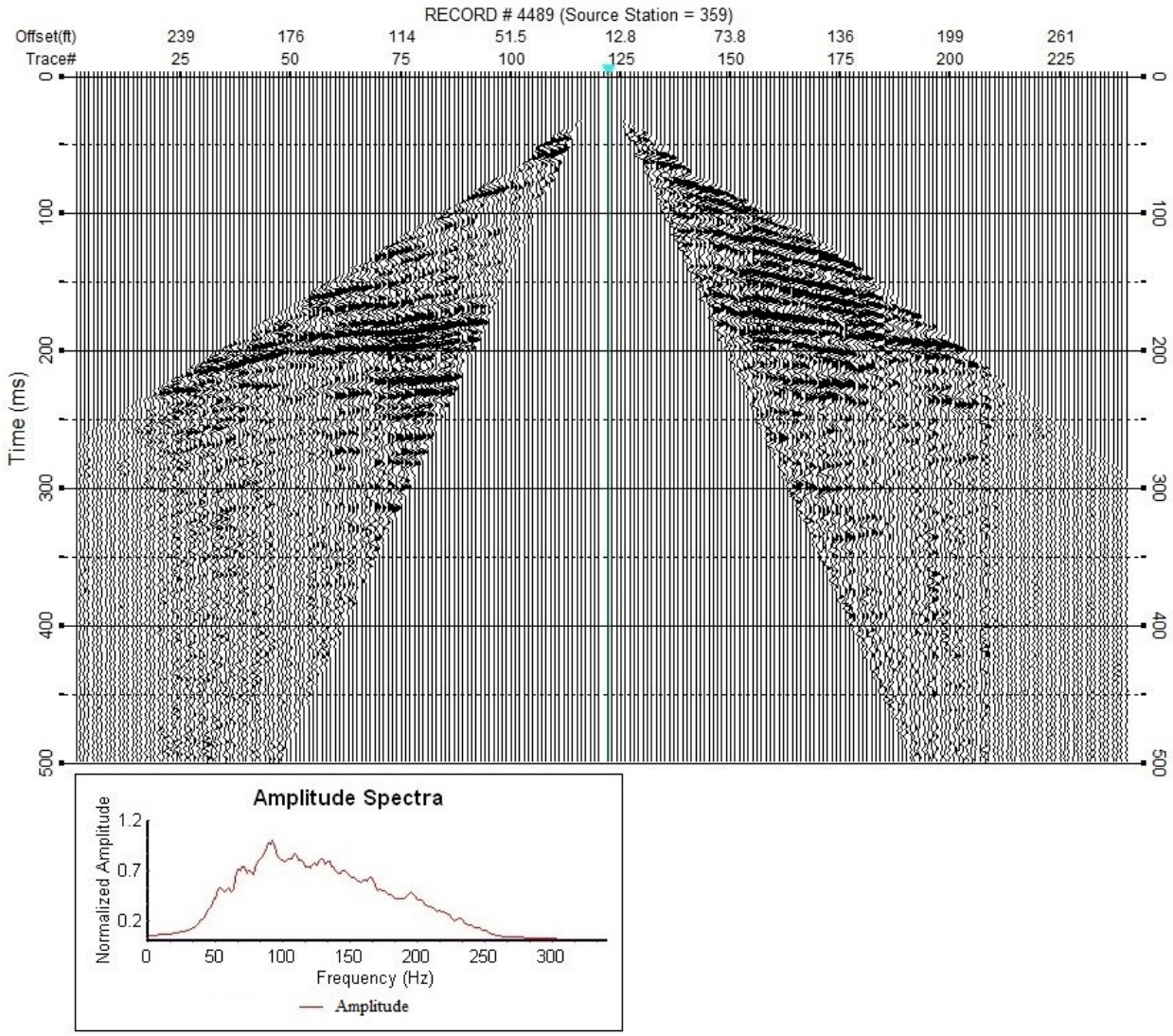

Figure 14. A processed vibroseis shot gather (top) and its spectrum (bottom). The spectrum of this record gather has a broad-frequency-band ranging from 0 Hz (DC) to 300 Hz.

Based on the velocity analysis and time migration it is suggested that there exists a high-velocity (3600 m/s) layer between 120 milliseconds – 175 milliseconds. This layer is located within the area bounded by the two red lines (**Figure 15**). This layer's interval velocity is calculated to be approximately 3600 m/s, which makes it consistent with the depth and velocity of the 'salt layer'. The interval velocity of this salt layer is higher than other layers bounding it and, of course, that is expected based on published salt vs. shale velocities. If a high-velocity layer varies laterally in thickness, it caused time image distortion ('pull-up' or 'sag' in time).

These features can result in loss of reflection continuity due to intraspread statics that are uncompensated for during routine processing. There are several of these velocity anomalies observed in the data (blue boxes in **Figure 15**) beneath this 'salt layer'. Also evident in these sample data is a low-velocity area between trace numbers 450 and 650 and between time 50 ms and 150 ms. It is reasonable to suggest this apparent structure may be the result of the deposition of sediment into a depression formed by the migration of a salt dissolution void toward the ground surface. Decreases in velocity due to these subsidence events will increase the travel time and cause time depression effects beneath the feature. All these velocity-related artifacts suggest that depth migration is needed to improve the image quality and accuracy. An interpreted section (**Figure 16**) provides a link between the processed reflection data with the geologic setting. Subsequence processes were applied to the time migration result (**Figure 15**) to produce this section. Displayed data in **Figure 16** were chosen between trace numbers 300 and 850 with a time range 0 ms to 300 ms. To reduce coherent high-frequency noises, a low-pass filter (high-cut frequency was set 150 Hz) was applied.

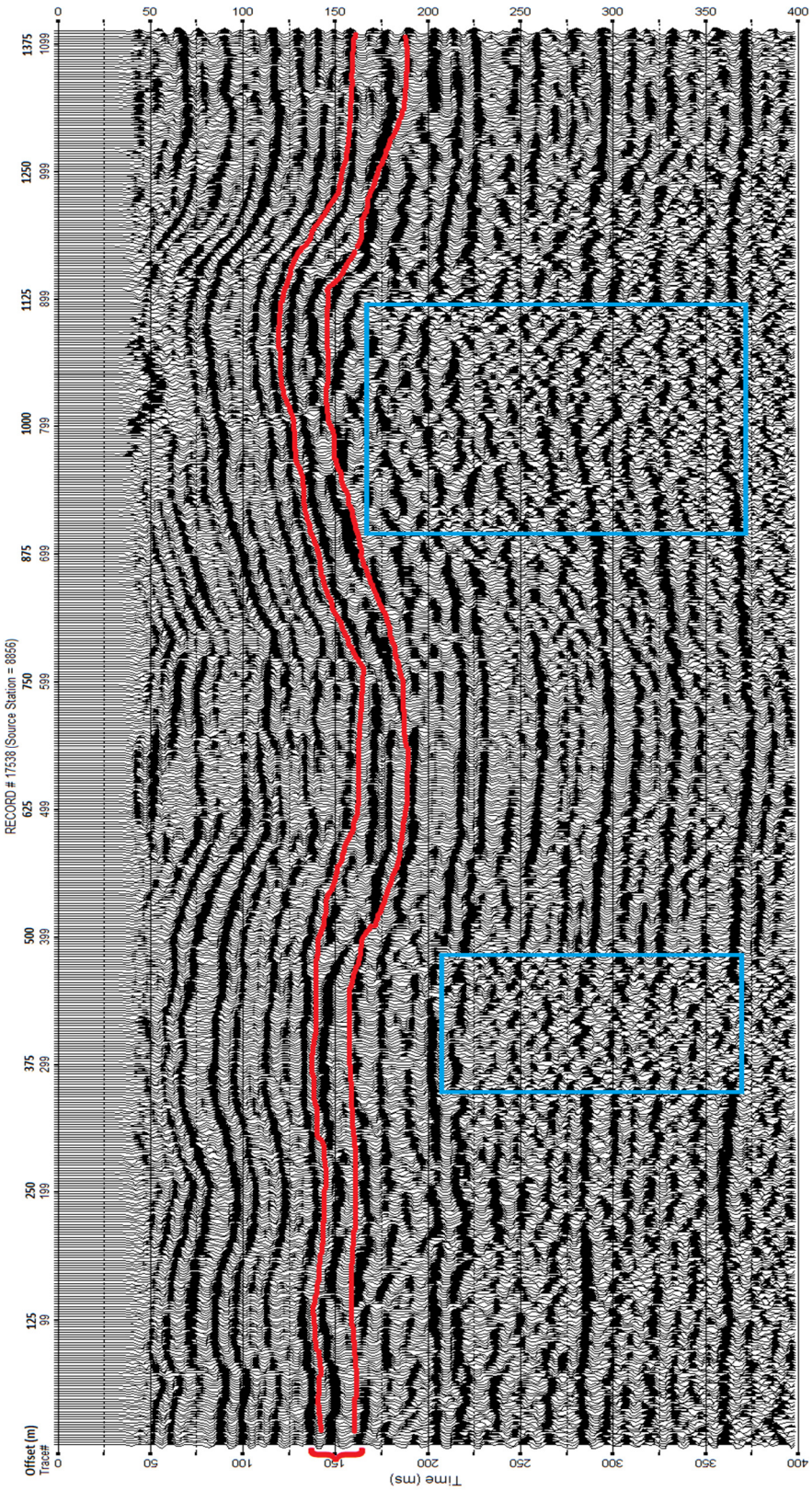

Figure 13. Time migrated section by using time domain F-K migration. A high-velocity layer is bounded by two red lines between 125 ms and 175 ms. Two areas showing lack of reflection continuity are closed up by blue boxes.

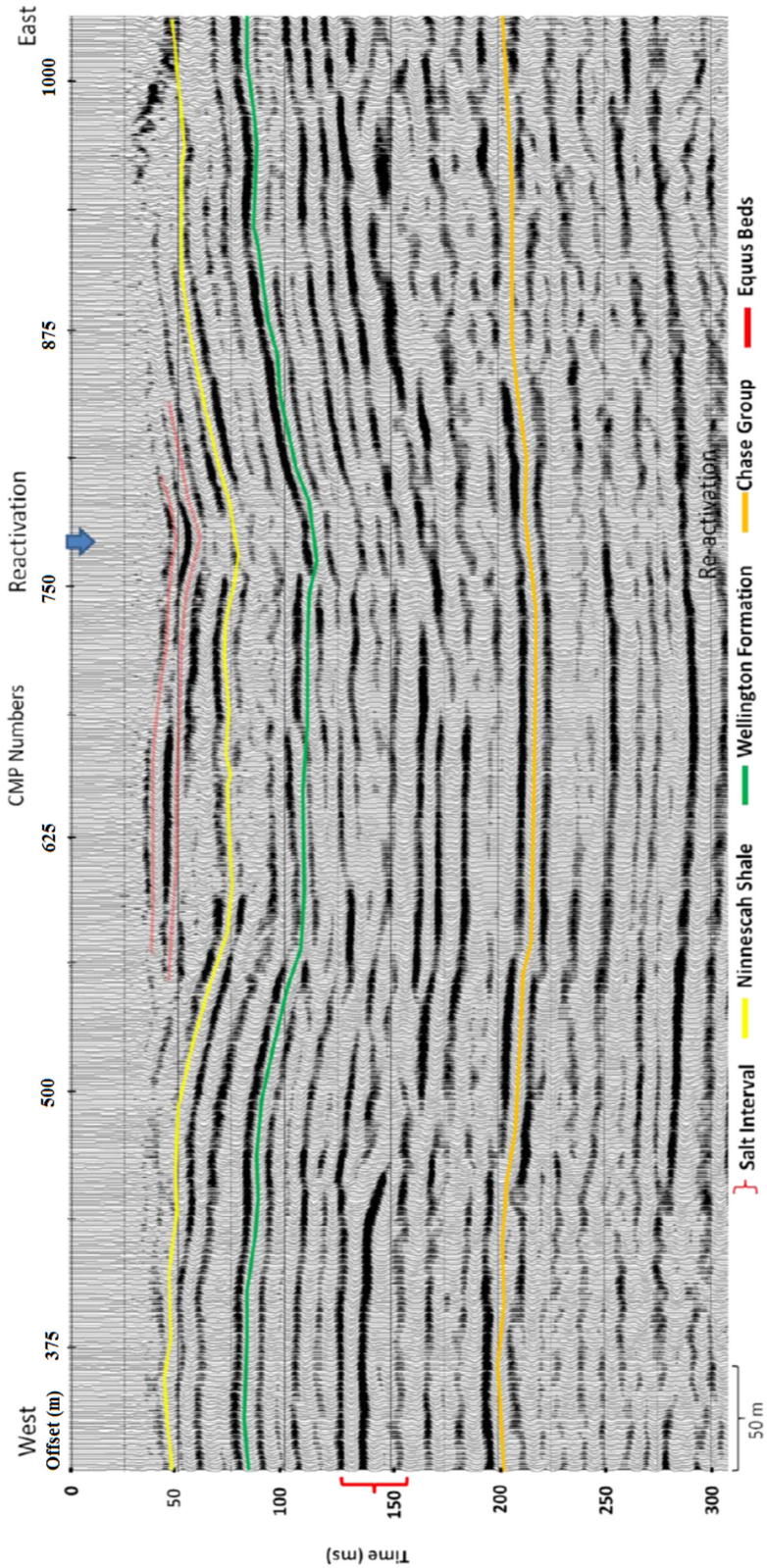

Figure 14. Interpretation of stacked CMP section (modified from Judy, 2015). Data were chosen from the time migration result (Figure 15) between trace numbers 300 and 850 with a time range 0 ms to 300 ms. To reduce coherent high-frequency noises, a low-pass filter (high-cut frequency was set 150 Hz) was applied.

Using the Dix equation (Dix, 1955)

$$V_{n-th\ layer} = \left(\frac{V_n^2 t_n - V_{n-1}^2 t_{n-1}}{t_n - t_{n-1}}\right)^{1/2}$$

the n-th layer interval velocity $V_{n-th\ layer}$ can be converted from the stacking velocities (RMS velocities) V_n and V_{n-1}. By interpolating the interval velocities calculated from the Dix equation, an initial velocity model (**Figure 17**) can be generated. The size of the velocity model is 1875 meters in x-direction (length) and 425 meters in z-direction (depth). Considering the problem of numerical stability of wavefield extrapolation, I set the space interval to be $dx = 2.5\ meters$ and $dz = 1.25\ meters$ (in x- and z-direction, respectively).

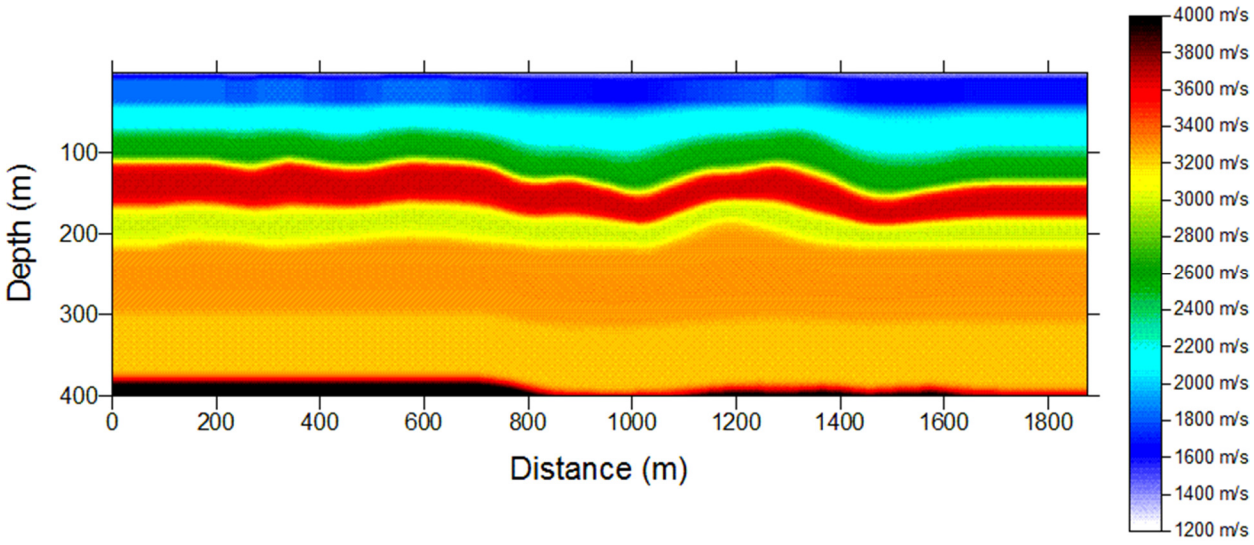

Figure 15. Initial velocity model.

5.2 Depth migration

Different migration methods have been applied to this h3east dataset using the same initial velocity model. A ray-tracing based Kirchhoff depth migration was applied (**Figure 18**). Comparing the result of the Kirchhoff depth migration with the time migration results (**Figure 15** and **Figure 16**) it is evident that the 'pull-up' and sag effects are reduced with the depth migration. Two distinct reflections, one at a depth of 250 meters (denoted with black arrows) and the other at

a depth of 375 meters, show improved continuity and appear flattened after depth migration. Considering the geologic setting, the change is reasonable and consistent with expectations.

From a resolution prospective, the results of the Kirchhoff depth migration are adequate for interpretation purposes at this location and for the defined goals. The 'h3east' Kirchhoff migration result (**Figure 18)** still possesses small discontinuities observed below 100 meters (red arrows). Corresponding areas in the time domain section have good continuity. As the time migration cannot image the faults as well as depth migration, it is needed to determine whether these small discontinuities are Kirchhoff migration artifacts or real faults.

To find out what are those discontinuities and improve resolution, I applied the RTM method to the h3east dataset. First a test was run using RTM with the Poynting-vector imaging condition applied to the data (**Figure 19)**. Then an RTM was applied with the band-selecting imaging condition (**Figure 20)**. These two data sets allow comparisons to be made to determine the effectiveness of versions of methods applied here.

First, I compare the result of RTM with Poynting-vector imaging condition (**Figure 19**) to Kirchhoff migration (**Figure 18**). After RTM it is hard to identify the previously noted small discontinuities or 'scatters' between 100 m and 400 m (red arrows) evident in the Kirchhoff migrated image. The layer at 250 meters depth (denoted with black arrows) is clearly well flattened and possesses good continuity. But in both the near-surface (less than 100m) and deep (deeper than 300m) zones, the image obtained using RTM with the Poynting-vector imaging condition does not appear to possess better continuity than that observed after Kirchhoff migration. At what is traditionally considered near-surface depths, the RTM image suffers from low-spatial-frequency artifacts. Compared to Kirchhoff migrated sections (**Figure 18)**, some of the obvious shallow layers (**Figure 19)** appear to be missing or attenuated. Within what I am

calling the shallow region, useful reflection signals are principally composed of the high-frequency components of the spectra. Because these high-frequency components are not dominant due to attenuation, they are indistinguishable after cross-correlation due to the high-amplitude nature of the low-frequency components. Within what I am calling the deep zones, comparing these RTM results to the Kirchhoff migration (**Figure 18)**, it is evident that the layer at 350m is not imaged with RTM using the Poynting-vector imaging condition (**Figure 19**). This is caused by cross-talk resulting from attenuated low-frequency components with embedded, coherent high-frequency noise. Taking into consideration these obvious drawbacks of the Poynting-vector imaging condition, it will be necessary to decompose the wavefield in the frequency domain before applying this imaging condition.

Finally, I applied my newly developed band-selecting imaging condition (**Figure 20)** to the RTM method. The spatial-dependent filter is defined using equations (15) and (18). Above depth 175 m the passing band frequencies were set to 80 Hz ~ 120 Hz with a low-cut frequency 50 Hz and a high-cut frequency 150 Hz. Below 175 m the passing band frequencies were set to 50 Hz ~ 150 Hz with a low-cut frequency 40 Hz and a high-cut frequency 200 Hz. A Cosine window was added to filters to avoid the Gibbs phenomenon. Compared to Kirchhoff migration and RTM with Poynting-vector imaging condition (**Figure 18** and **Figure 19)**, band-selecting RTM appears to possess higher resolution in both the near-surface and deep zones. Within the near-surface, the low-spatial-frequency artifacts are suppressed and layers have good continuity. Expected and very realistic structures like faults and folds can now be identified and deep layers appear to flatten through removal of discontinuities in a fashion consistent with the local and regional geology.

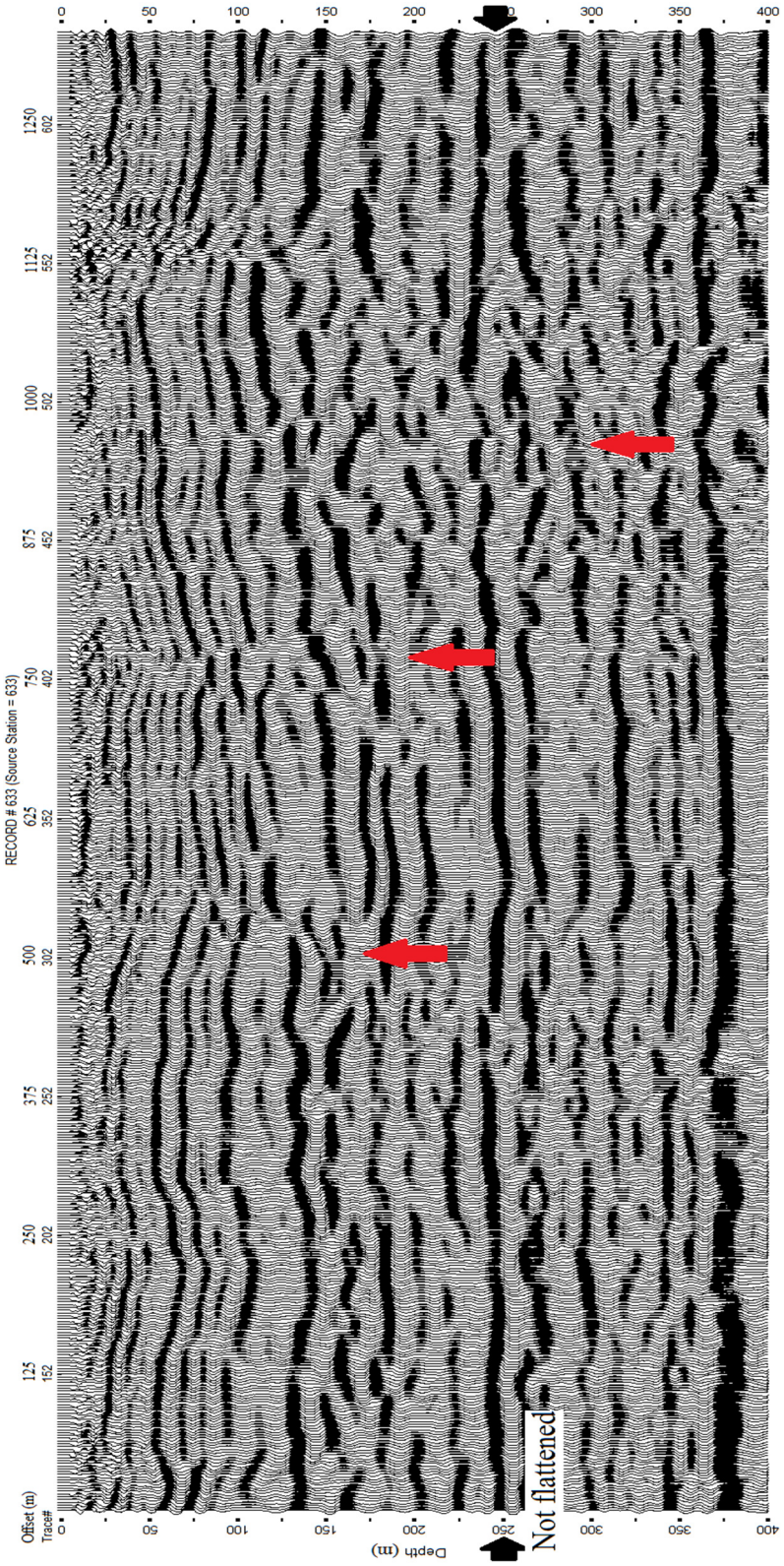

Figure 16. Kirchhoff depth migration. Small discontinuities are identified with red arrows. These discontinuities are not obvious in the time migration results (Figure 15 and 16). Reflections from layer at 250 m depth (denoted with black arrows) are not flattened.

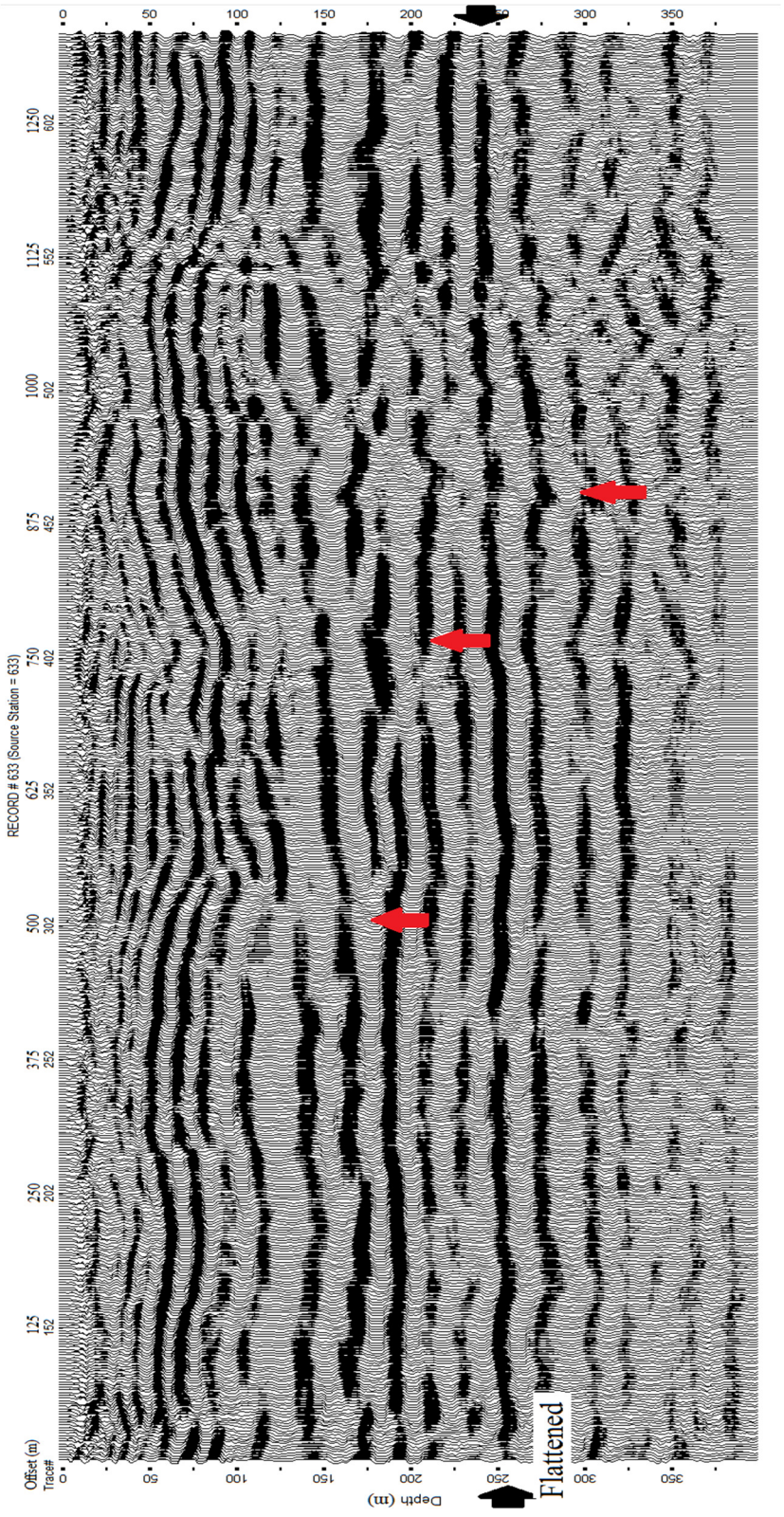

Figure 17. RTM using Poynting-vector imaging condition. Red arrows denote areas where Figure 18 shows discontinuities. Reflections from layer at 250 m depth (denoted with black arrows) are well flattened.

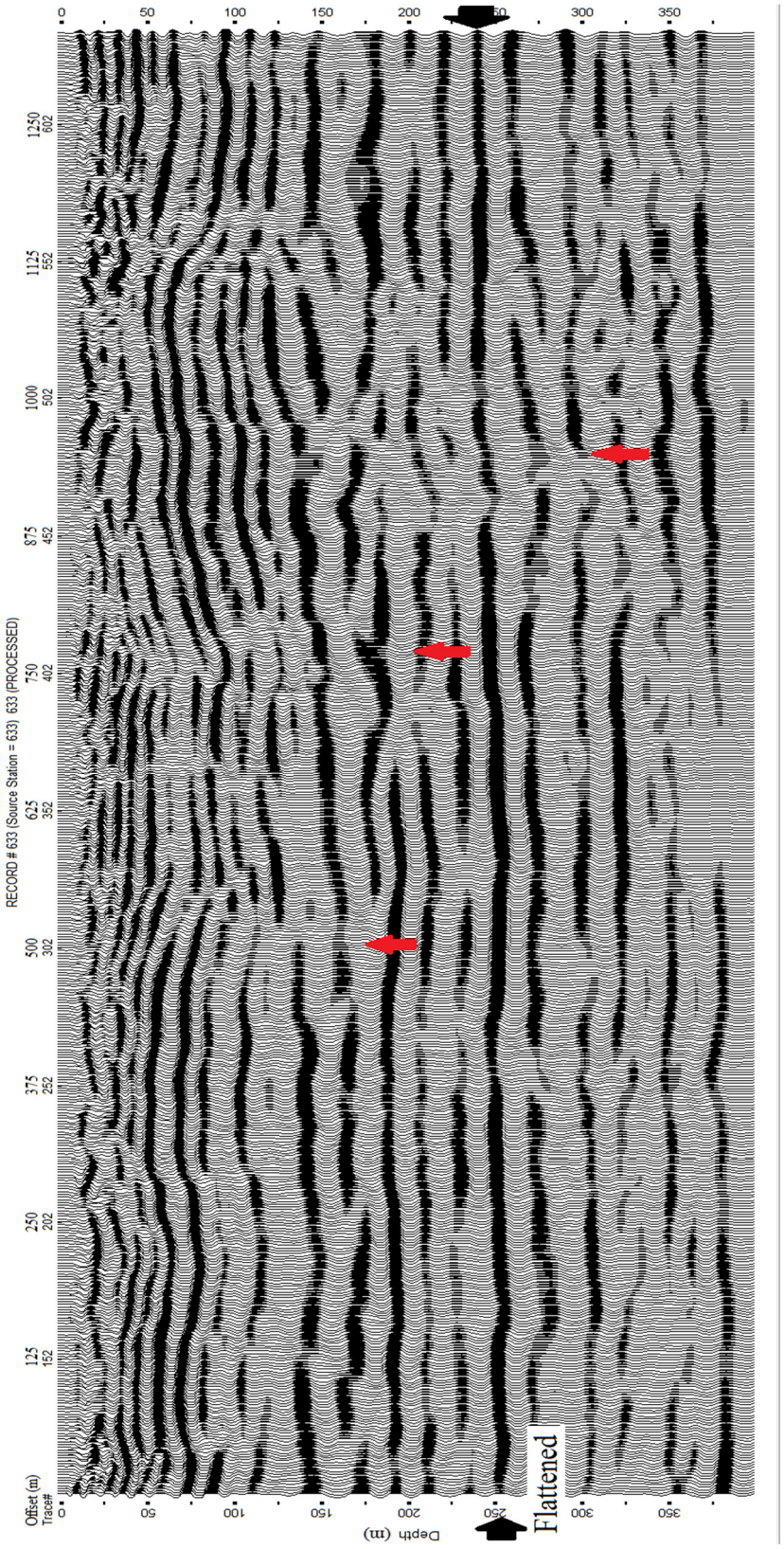

Figure 18. RTM using band-selecting imaging condition. Red arrows denote areas where Figure 18 shows discontinuities. Reflections from layer at 250 m depth (denoted with black arrows) are well flattened.

The results presented and compared here have demonstrated that the band-selecting imaging condition is superior to the Poynting-vector imaging condition in suppressing the low-spatial-frequency artifacts prevalent in near-surface reflection sections. The frequency spectra of these three migration results demonstrate the improved resolution (**Figure 21**). Comparing figures highlighting the same part of each migrated data set (**Figure 21**), it is evident that RTM with band-selecting imaging condition is superior to the other two methods in imaging shallow structures and suppressing artifacts.

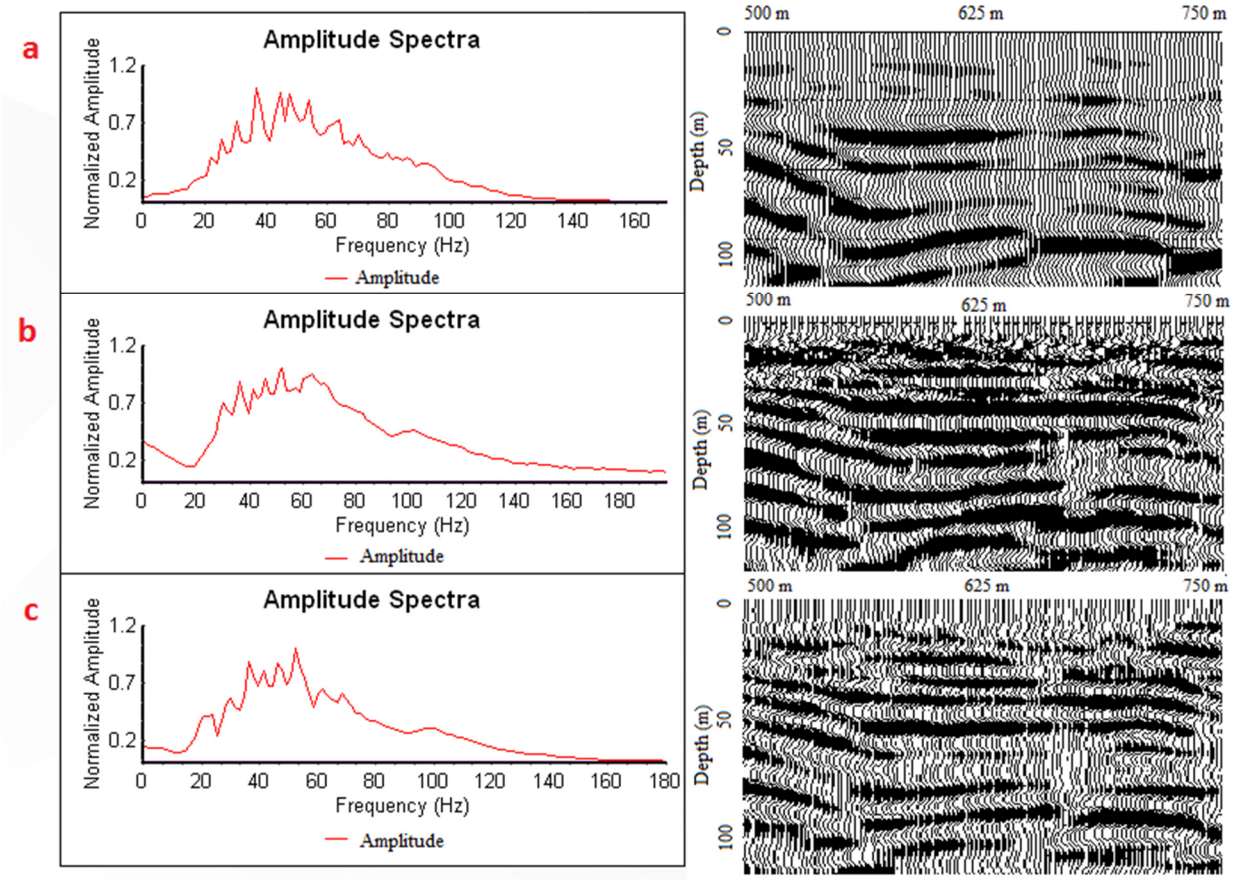

Figure 19. Frequency spectra (left) of migration results. a) Spectrum of Kirchhoff depth migration. b) Spectrum of RTM with Poynting-vector imaging condition. The low-frequency artifact can be identified. c) Spectrum of RTM with band-selecting imaging condition. It can be observed that the low-frequency artifacts got suppressed. From figures of the same part of each migrated data (right) it can be determined that RTM with band-selecting imaging condition are superior to the other two methods in imaging shallow structures and suppressing artifacts.

It is necessary to mention that all these three migration results use the same velocity model (**Figure 17**). So these results are actually preliminary results. The standard migration procedure

includes velocity model correction and updating. If more iterations were taken the results would improve, with the frequency band-selecting method becoming more obviously the superior approach. But considering the purpose of this study is to demonstrate the effectiveness of band-selecting imaging condition to improve imaging quality in the near-surface, these preliminary results adequately meet the requirement.

6 - Interpretation

In this chapter I interpret the depth migrated data ('h3east'). The migrated seismic profiles are interpreted in a stretched spatial domain or in a converted depth domain. To facilitate this transformation, the migrated traces were converted from depth to time using the laterally averaged stacking velocity function. This velocity function is the average value of all the individual velocity functions evaluated at each middle point. It is laterally homogeneous and has no physical meaning, but provides a meaningful domain to evaluate these methods. This average stacking velocity function is then used for stretching the depth migration result. This stretched result is convenient for identifying layers and structures when this result is compared with the time migration results.

Studying the time migration result (**Figure 22**) of the 'h3east' dataset, it is obvious that below 150 ms there are three main reflection intervals identifiable on the time migration sections. These intervals are: the top of the Ninnescah shale (denoted by a yellow line), the top of the Willington formation (denoted by a green line), and the top of Chase group (denoted by an orange line). The top and base of the salt interval is between the Willington Formation and the Chase group. Due to lack of trace continuity, the salt interval has not been highlighted on these sections. On the migrated section, almost all the reflections below the base of the salt are subparallel. Based on the geology background, these parallel layers beneath the base of the salt are expected to be flat and cyclic. I use that premise during the velocity model building segment for these layers and

therefore have some influence on keeping them relatively flat. Adjustment can be made to the velocity model, allowing variability in the relative structure, with iterations of the migration operation converging on the ideal set of parameters. The depth migrated section can be examined to confirm this assumption is reasonable.

Time domain converted results of the RTM (**Figure 23**) demonstrate the utility of the method with significantly more structures evident in the near-surface than the section from time migration (**Figure 22**). The reason for this is that, unlike the NMO correction, RTM is a wave equation migration method that does not assume reflectors to be flat, and therefore provides a much better and more representative image than other methods. By computing the full wavefield at each grid point of the velocity model, the full wavefield can be simulated for the entire image by summing along the two-way raypath. Thus, more structural details can be imaged through RTM. In the RTM section some of the faults (denoted by blue lines) are much easier to identify, although many are not apparent at all in the time migration result. This comparison emphasizes the necessity of applying depth migration to the shallow reflection datasets. Beneath the salt layer reflections appear flat, as is both expected and consistent with drill based models. Compared to the time migrated section, the velocity variation artifacts are reduced and reflection continuity is noticeably improved. This migration approach does not correctly relocate every reflection event, so there still exist a few discontinuities and structural artifacts. These undercorrected reflections are due to busts in the initial velocity model, not artifacts generated by the migration algorithm. It is, therefore, a future direction for my research, to incorporate RTM with iterative velocity analysis to dramatically improve the high fidelity nature of the 3-D velocity function over current velocity analysis routines.

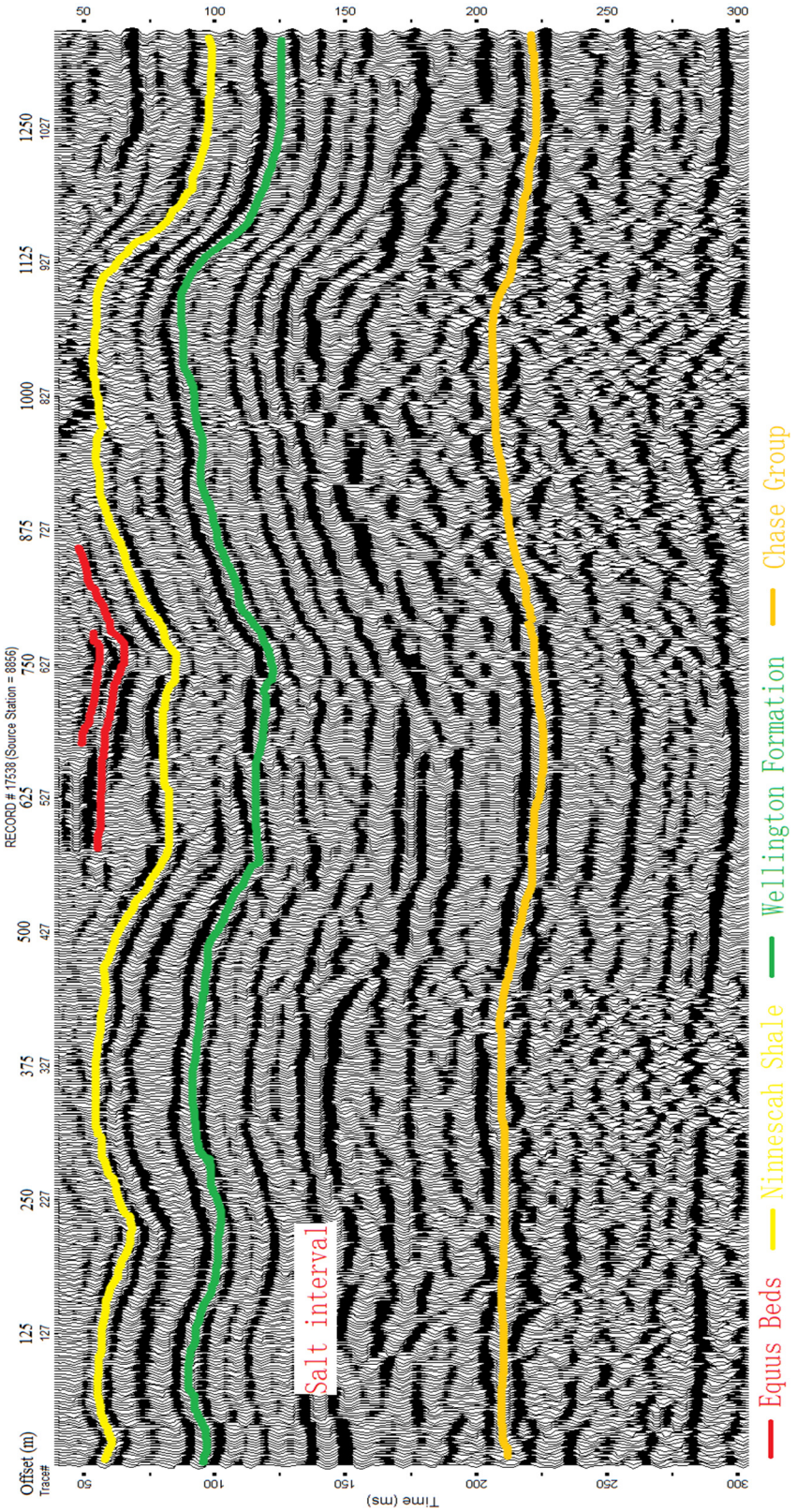

Figure 20. Time migration result.

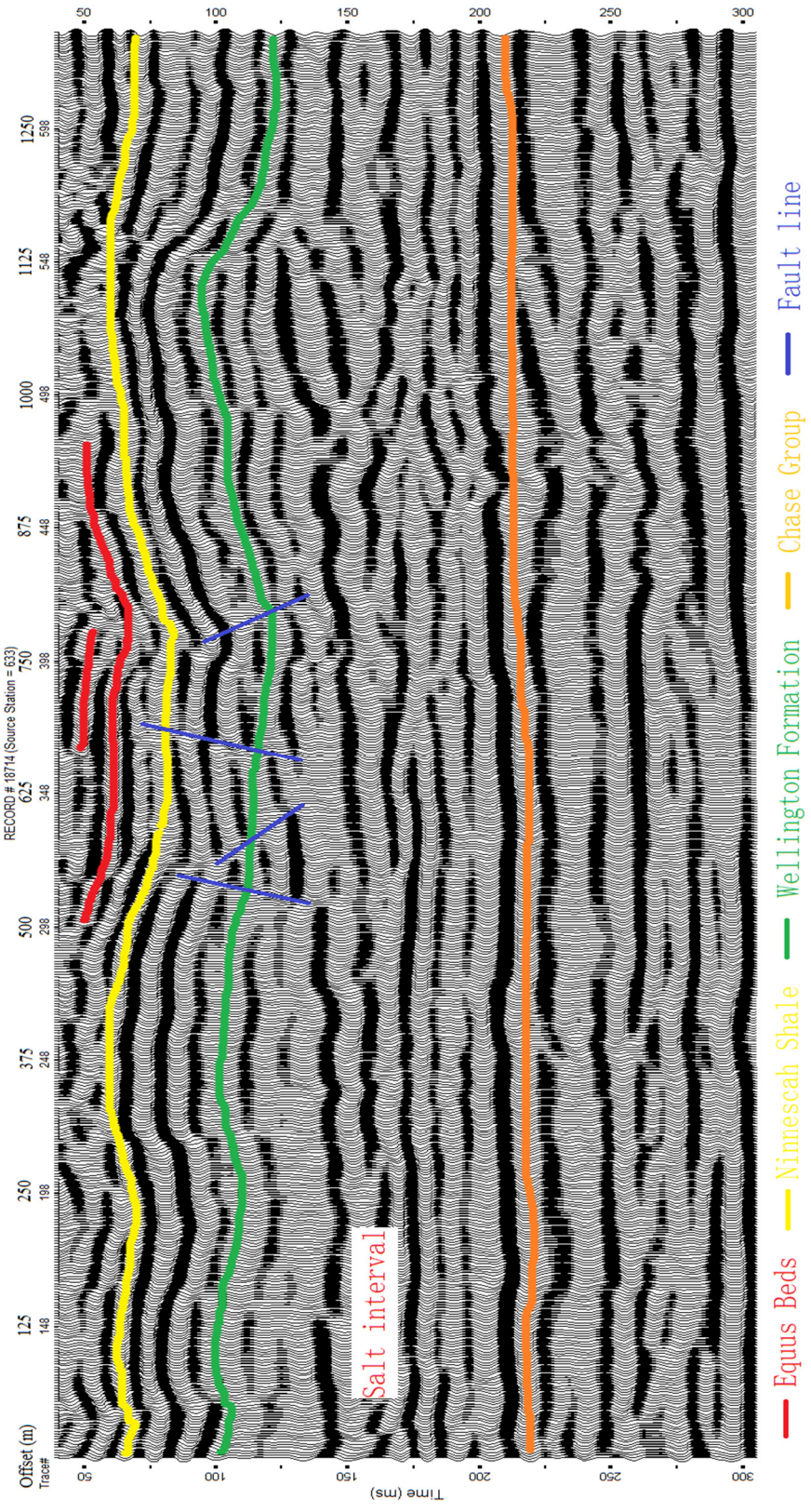

Figure 21. RTM result convert into time domain.

Although not a perfect representation of the subsurface, this preliminary migration result possesses greater resolution within the near-surface and provides better trace-to-trace continuity with less noise compared to either the Kirchhoff migration or RTM with Poynting-vector or correlation-based imaging condition. This result suggests that an effective velocity model-correcting process that allows updating of the interval velocities is needed for practical and accurate application of shallow seismic migration. The discussion of this point involves future works and will be presented in chapter 7.

7 - Discussion

I have shown that the resolution of near-surface seismic migration can be increased using RTM with a band-selecting imaging condition that decomposes the wavefield in the frequency domain. Effectively, I have introduced a practical method of suppressing the low-spatial-frequency artifact prominent with other methods. When applying this method, a spatial-dependent frequency filter is defined with each update in the velocity model. In the imaging procedure, this filtering technique decomposes the wavefield at each image grid point so only the frequencies that match the user-defined criteria (equation (15)) are permitted into the cross-correlation stage. Within the near-surface, where high-frequency components of the reflection wavelet are considered more valuable than low-frequency components, this filtering technique can reduce the influence of low-frequencies and therefore the cross-correlation of high-frequency signals is strengthened with artifacts reduced.

Both of the numerical experiments and the field data processing described here demonstrate that this band-selecting imaging condition is effective in suppressing low-spatial-frequency artifacts. Moreover, this method is not computationally expensive when the RTM is performed in the frequency domain. Wavefield extrapolation in the frequency domain preserves

the wavefield with respect to frequencies present. So, during the imaging procedure the wavefield data at different frequencies populate each grid point and are then filtered at each grid point. This operation adds very little computation time. But if the wavefield extrapolation is performed in time domain—which means the wavefield is preserved based on time sampling—the wavefield must be transformed into the frequency domain at every grid point first. In this time domain situation, reading in data and then running a Fourier transform on each data point would require large capacity computational resources. Therefore, it is strongly recommended that the RTM be performed in the frequency domain.

Another purpose of this research was to begin the development of a reverse time migration method that is ideally suited for shallow seismic reflection datasets. That is a future direction of this work that now has a strong foothold with the findings I have reported in this thesis. In this research I found that iterative migration/velocity function updates may be a solution to optimistically migrate shallow datasets. Multiple methods can be used to generate reasonable initial models. These initial models could be produced using full waveform inversion (Tarantola, 1984) or tomography. After the initial velocity model is generated, a preliminary result can be obtained and for many cases that will suffice. If better resolution and accuracy is needed, then the preliminary migrated data can be sorted into traces to form a common image gather (either in offset domain or in angle domain) and wave equation migration velocity analysis (WEMVA) (Biondi and Sava, 1999) can be applied to update the model. Another iteration can begin with this updated velocity model. The migration/velocity update loop can stop when the correction of the velocity model is sufficiently small or convergence cannot be improved any further. The output of this migration loop is an updated velocity and a migrated seismic profile. That is the process that will

likely extend research reported here toward a more accurate shallow seismic image and eventually computationally efficient full waveform inversion (FWI).

8 - Conclusion

The band-selecting imaging condition introduced here effectively suppresses the low-spatial-frequency artifact of RTM and dramatically improves shallow seismic image potential through accurate migration. Based on this imaging condition, a high-resolution near-surface reflection migration method can be applied to even the most structurally complex settings. Testing this method on both synthetic data and field data show that this unique imaging condition provides highly accurate images of structural complexities.

The present code developed for this method requires a spatial-dependent filter (equation (15)). This criterion may not be well suited for some geologic environments, such as gradually changing velocities that produce weak reflections. In practice, the thickness of an individual layer is hard to estimate due to the heterogeneity of rock, heterogeneities that manifest themselves as subspread velocity variability. One way to solve this problem is the comb-filter (Chu and Burrus, 1984), designed to decompose the wavefield into narrow-frequency-band components. Then frequencies used for imaging can be chosen from these narrow frequency bands.

For efficiency the code developed for this work requires the RTM operate in the frequency domain. This is a beneficial characteristic of this method because frequency domain RTM is more computationally efficient than time domain RTM when the code is parallelized. As frequency domain RTM gets more popular, the band-selecting imaging condition will be an even more important and noted contribution to the science.

9 - References

Baher, Hussein. *Analog and digital signal processing*. John Wiley & Sons, 2001.

Bayne, C.K., 1956, Geology and ground-water resources of Reno County, Kansas: Kansas Geological Survey, Bulletin 120.

Baysal, E., Kosloff, D.D., and Sherwood J.W.C., 1983, Reverse time migration. Geophysics, 48(11): 1514-1524.

Baysal, E., Kosloff, D.D., and Sherwood J.W.C., 1984, A two-way nonreflecting wave equation. Geophysics, 49(2): 132-141.

Berkhout, A.J., 2012, Combining full wavefield migration and full waveform inversion, a glance into the future of seismic imaging. Geophysics, 77(2): S43-S50.

Biondi, B., and Sava, P., 1999, Wave-equation migration velocity analysis. 69th Ann. Internat. Mtg Soc. of Expl. Geophys, p. 1723-1726.

Bradford, J.H., Liberty, L.M., Lyle, M.W., et al., 2006, Imaging complex structure in shallow seismic-reflection data using prestack depth migration. Geophysics, 71(6): B175-B181.

Chang, W.F., McMechan, G.A., 1986, Reverse-time migration of offset vertical seismic profiling data using the excitation-time imaging condition. Geophysics, 51(1): 67-84.

Chattopadhyay, S., McMechan, G.A., 2008, Imaging conditions for prestack reverse-time migration. Geophysics, 73(3): S81-S89.

Chu, S., Burrus, C.S., 1984, Multirate filter designs using comb filters. Circuits and Systems, IEEE Transactions, 31(11): 913-924.

Dellwig, L.F., 1971, Study of salt sequence at proposed site of the national radioactive waste repository at Lyons, Kansas;. In Final Report, Geology and Hydrology of the proposed

Lyons, Kansas Radioactive Water Repository Site: Kansas Geological Survey, Subcontract No. 3484.

Diaz, E., and Sava, P., 2012, Understanding the reverse time migration backscattering: noise or signal. SEG Technical Program Expanded Abstracts: 1-6.

Dix, C.H., 1955, Seismic velocities from surface measurements: Geophysics, 20, 68–86.

Etgen, J.T., 1986, High-order finite-difference reverse time migration with the 2-way non-reflecting wave equation: Stanford Exploration Project Report, 48, 133-146.

Etgen, J.T., 1986, Prestack reverse time migration of shot profiles. SEP-50, 151-170, Available at http://sep.stanford.edu/research/reports.

Farmer, P., Zhou, Z.Z., and Jones, D., 2009, The role of reverse time migration in imaging and model estimation. The Leading Edge, 28(4): 436-441.

Fletcher, R.F., Fowler, P., Kitchenside, P., et al., 2005, Suppressing artifacts in prestack reverse time migration. SEG Technical Program Expanded Abstracts.

Fleury, C., and Vasconcelos, I., 2012, Investigating an Imaging Condition For Nonlinear Imaging-Principles And Application to Reverse-time migration Artifacts Removal.SEG Technical Program Expanded Abstracts.

Fleury, C., and Vasconcelos, I., 2013, Adjoint-state reverse time migration of 4C data: Finite-frequency map migration for marine seismic imaging. Geophysics, 78(2): WA159-WA172.

Gogel, T., 1981, Discharge of Saltwater from Permian Rocks to Major Stream-aquifer Systems in Central Kansas: Chemical Quality Series 9.

Guan, H., Kim, Y.C., Ji, J., et al., 2009, Multistep reverse time migration. The Leading Edge, 28(4): 442-447.

Guitton, A., Kaelin, B., and Biondi, B., 2006, Least-square attenuation of reverse time migration artifacts. SEG Technical Program Expanded Abstracts.

Judy, B., 2015, High resolution seismic reflection to characterize small scale mechanisms of large scale natural dissolution in the Hutchinson Salt Member, Master's Thesis, University of Kansas.

Levin, S.A., 1984, Principle of reverse-time migration. Geophysics, 49(5): 581-583.

Li, J., Yang, D., Liu, F., 2012, An efficient reverse time migration method using local nearly analytic discrete operator. Geophysics, 78(1): S15-S23.

Liu, F., Zhang, G., Morton, S.A., et al., 2011, An effective imaging condition for reverse-time migration using wavefield decomposition. Geophysics, 76(1): S29-S39.

Liu, Y., Chang, X., Jin, D., et al., 2011, Reverse time migration of multiples for subsalt imaging. Geophysics, 76(5): WB209-WB216.

Merriam, D.F., 1963, The Geologic History of Kansas: Kansas Geological Survey, Bulletin 162.

Miller, R.D., and R. Henthorne, 2004, High-resolution seismic reflection to identify areas with subsidence potential beneath U.S. 50 Highway in eastern Reno County, Kansas: Proceedings of the 55th Highway Geology Symposium, September 8-10, Kansas City, Missouri, p. 29-48.

Miller, R.D., 2007, High-resolution seismic investigation of subsidence from dissolution: PhD. Dissertation, University of Leoben.

Nguyen, B.D., and McMechan, G.A., 2012, Excitation amplitude imaging condition for prestack reverse-time migration. Geophysics, 78(1): S37-S46.

Norton, G.H., 1939, Permian redbeds of Kansas. Wichita, Kansas: American Association of Petroleum Geologists.

Steeples, D.W., and R.D. Miller, 1998, Avoiding pitfalls in shallow seismic surveys. Geophysics, p 1213-1224.

Tarantola A., 1984, Inversion of seismic reflection data in the acoustic approximation. Geophysics, 49(8): 1259-1266.

Ver Wiebe, W.A., 1937, Wichita Municipal Univ. Bull., v. 12, no. 5.

Walters, R.F., 1978, Land subsidence in central Kansas related to salt dissolution: Kansas Geological Survey Bulletin 214.

Watney, W.L., Nissen, S.E., Bhattacharya, S., and Young, D., 2003, Evaluation of the role of evaporite karst in the Hutchinson, Kansas, gas explosions, January 17 and 18, 2001; in K.S. Johnson and J.T. Neal, eds., Evaporite karst and engineering/environmental problems in the United States: Oklahoma Geological Survey Circular 109, p. 119-147.

Wang, B., Mason, C., Guo, M., et al., 2009, Subsalt velocity update and composite imaging using reverse-time-migration based delayed-imaging-time scan. Geophysics, 74(6): WCA159-WCA166.

Weibull, W.W., Arntsen, B., 2013, Automatic velocity analysis with reverse-time migration. Geophysics, 78(4): S179-S192.

West, R., Miller, K.B., and Watney, W.L., 2010, The Permian System in Kansas: Kansas Geological Survey Bulletin 257.

Yilmaz Ö. Seismic data analysis [M]. Tulsa: Society of exploration geophysicists, 2001.

Yoon, K, and Marfurt, K.J., 2006, Reverse-time migration using the Poynting vector. Exploration Geophysics, 37(1): 102-107.